Arch Appl Mech (2011) 81: 1093–1116
DOI 10.1007/s00419-010-0468-x

ORIGINAL

**Reza Mirzaeifar · Mahmoud Shakeri · Reginald DesRoches · Arash Yavari**

# A semi-analytic analysis of shape memory alloy thick-walled cylinders under internal pressure

Received: 8 April 2010 / Accepted: 5 August 2010 / Published online: 28 August 2010


**Abstract** In this paper, a new method for analysis of the pseudoelastic response of shape memory alloy thick-walled cylinders subjected to internal pressure is proposed. Two cases of short and long cylinders are considered by assuming the plane stress and plane strain conditions. In each case, a three-dimensional phenomenological SMA constitutive model is simplified to obtain the corresponding two-dimensional constitutive relations. The cylinder is partitioned into a finite number of narrow annular regions, and appropriate assumptions are made in order to find a closed-form solution for the equilibrium equations in each annular region. The global solution is obtained by enforcing the stress continuity condition at the interface of the annular regions and imposing the boundary conditions. Several numerical examples are presented to demonstrate the efficiency of the proposed method, and the results are compared with three-dimensional finite element simulations.

**Keywords** Shape memory alloy (SMA) · Thick-walled cylinder · Pseudoelastic · Internal pressure

## 1 Introduction

Considerable increase in the use of active (multifunctional) materials in recent years has led to an excessive interest in analysis of different types of active materials in various shapes. Among several types of active materials, shape memory alloys (SMAs) have been extensively studied and have also been used in a wide variety of applications ranging from biomechanics [30] to aerospace [10], and civil engineering [6]. The widespread use of SMAs is mainly because of their unique ability in generating relatively large inelastic deformations and high stresses. Distinctive properties of SMAs are a consequence of their ability in changing their crystallographic structure between a high symmetry parent phase (austenite) and a low symmetry phase (martensite) in response to mechanical and/or thermal loads. For a comprehensive discussion on general properties of SMAs and the phase transformation phenomenon, readers are referred to Müller and Xu [17], Müller and Seelecke [24], Lagoudas [25], and Mirzaeifar et al. [22].

The transformation between the two stable phases, called martensitic phase transformation, results in significant challenges in introducing realistic constitutive relations for shape memory alloys. Although there are some micromechanical approaches in developing SMA constitutive relations [28,29], macroscopic phenomenological models are more common in practice due to their compatibility with numerical methods. These

R. Mirzaeifar
George W. Woodruff School of Mechanical Engineering, Georgia Institute of Technology, Atlanta, GA 30332, USA

M. Shakeri
Mechanical Engineering Department, Amirkabir University of Technology, Tehran, Iran

R. DesRoches · A. Yavari (✉)
School of Civil and Environmental Engineering, Georgia Institute of Technology, Atlanta, GA 30332, USA
E-mail: arash.yavari@ce.gatech.edu

models are based on continuum thermomechanics and construct a macroscopic free energy potential depending on the state and internal variables used to describe the measure of phase transformation. Consequently, evolution equations are postulated for the internal variables and the Second Law of Thermodynamics is used in order to derive constraints on the material constitutive equations. In recent years, different constitutive models have been introduced by different choices of internal state variables and their evolution equations. Among the most widely accepted models, we can mention the cosine model [20], the exponential model [34], and the polynomial model [4]. Lagoudas et al. [15] unified these models using a thermodynamic framework.

Highly non-linear coupled material response of SMAs—a consequence of the solid-to-solid phase transformation—restricts the applicability of the available solution methods for analysis of many SMA structures among which finite element method is the most common. There are rare attempts for analyzing even simple SMA structures using analytical or semi-analytical methods. The availability of closed-form solutions for SMA structures is primarily affected by the constitutive relations in use. In addition to the constitutive relations, the complexity of the structure can play a key role in finding closed-form solutions. Lagoudas et al. [16] presented a one-dimensional reduction of the unified SMA constitutive relations of Lagoudas et al. [15] and using this model proposed closed-form expressions for the martensitic volume fraction and transformation strains in uniaxial loading of an SMA prismatic bar. However, an explicit constitutive relation for the axial stress component as a function of axial displacement was not introduced; a numerical method was necessary for solving the loading/unloading response of bars (see [17]). They used this solution technique in conjunction with finite element method for dynamic analysis of polycrystalline SMA rods. Feng and Sun [7] presented an algorithm for analyzing shakedown of SMA structures subjected to cyclic or varying loads. They used a plasticity framework and calculated a lower bound of loads for transformational shakedown of SMAs without the necessity of a step-by-step analysis along the loading history.

In another attempt for finding semi-closed-form solutions for two-dimensional SMA structures, Birman [1] considered an infinite shape memory alloy plate with a circular hole subjected to biaxial tensile stresses applied at infinity. The solution was obtained by the plane stress assumption based on the two-dimensional form of Tanaka's constitutive relations [33]. He presented two different solutions for stress analysis that are called by him "closed-form-solution" and "exact solution". In the latter, it is assumed that for the SMA with phase transformation, the ratio of the radial to circumferential stress is identical to that in the elastic case. As it will be shown in this paper, this assumption cannot be justified. In the "closed-form" solution, there are some unrealistic simplifying assumptions; the elastic stress distribution in the region in which phase transformation has started is considered for calculating the inner boundary of pure austenite region. As we will show shortly, this assumption can be used only for some specific loading conditions and by spread of the transformed region this assumption becomes less and less accurate. Additionally, in Birman's closed-form solution, for obtaining the stress-strain relations, the transformation strains are related to the martensitic volume fraction by constant multipliers. Although this assumption remarkably simplifies the solution, it can be replaced by a more realistic formulation that will be presented in this paper. One of the main challenges in obtaining closed-form solutions for structures made of phase transforming materials is introducing an accurate solution for the regions that are completely transformed to martensite. Although the response of the structure is elastic for the fully martensite regions, it is necessary to consider the history of loading and the final values of transformation strain components to obtain the solution in these regions. In the present semi-analytic analysis, we will explain how to obtain the solution for these regions.

In a recent attempt, Mirzaeifar et al. [23] developed an exact solution for pure torsion of shape memory alloy circular bars. A general three-dimensional constitutive relation for shape memory alloys was first reduced to an appropriate one-dimensional form suitable for pure torsion. An explicit expression was derived for shear stress as a function of geometric specifications, material constants, and shear strain that enabled the solution to be obtained analytically. Response of circular bars in torsion was then analyzed by considering different possibilities that may happen in various loading levels.

Among various shapes in which SMAs are used, cylindrical shells are of particular interest in applications including spinal vertebrae spacers [21], special cardiovascular stents [14], and active catheters [18], which are in the form of thin shells. Li and Sun [19] studied the superelastic response of nano-grained SMA microtubes under uniaxial tension. Their experimental results show that the nucleated macroscopic martensite band in a microtube under uniaxial loading takes the shape of a spiral that surrounds the tube axis for several circles. Feng and Sun [8] studied the response of SMA microtubes subjected to a combined tensile and torsional loading experimentally. He and Sun [11] studied the effect of tube geometry on the helix-shaped deformation domains that are observed in SMA tubes during the stress-induced martensitic phase transformation of the material under uniaxial stretching.

In this paper, SMA thick-walled cylinders are considered. Two extreme cases of long and short cylinders can be reduced to plane strain and plane stress, respectively. SMA short cylinders or rings have many engineering applications, e.g. the SMA pipe couplings [5,12], tube wall joints [35], and active stiffener strips [13]. Shape memory alloys have suitable mechanical characteristics that make them desirable in pressure vessels and pipes as active layers, which are in the form of long thick cylinders [26,27].

In the present study, SMA short and long thick-walled cylinders are considered. For short cylinders in the form of a ring or stiffener strip, in the absence of axial forces, plane stress condition is a good approximation. Long cylinders can be reduced to a plane strain problem. Using these assumptions, the three-dimensional problem is reduced to a two-dimensional one. Constitutive equations are reduced to appropriate two-dimensional relations, and an explicit expression is obtained for the martensitic volume fraction and transformation strains in both cases. The cylinder is partitioned into a finite number of annular regions, and simplifying assumptions are made in each annular region in order to obtain an explicit expression for the stress components as functions of displacements. These stress-displacement expressions are then used to write the equilibrium equations in terms of radial displacements in each annular region. The global solution for the cylinder is finally obtained by putting the solutions of annular regions together and by enforcing the continuity conditions at the interfaces and at the inner and outer boundary regions. Our semi-analytic approach can be used to validate numerical methods like the finite element method.

This paper is organized as follows. In Sect. 2 a general three-dimensional constitutive equation for polycrystalline SMAs is briefly reviewed. Three dimensional constitutive relations are reduced to plane strain and plane stress constitutive equations in Sect. 3, and explicit expressions are given for the martensitic volume fraction in both cases. The internal pressure corresponding to the initiation of phase transformation is also obtained in Sect. 3. In Sect. 4, the transformation strain components in both plane stress and plane strain are presented. The semi-analytic solution for the case in which the inner radius is not completely transformed to martensite is given in Sect. 5, and the same solution for cylinders with completed phase transformation at the inner radius is given in Sect. 6. A step-by-step solution procedure is described in Sect. 7. Section 8 presents some numerical examples demonstrating the efficiency of the semi-analytic solution and a comparison with the results of three dimensional finite element simulations. Conclusions are given in Sect. 9. In the appendix, a sensitivity analysis is presented for calculating the appropriate number of annular regions and loading steps in the semi-analytic solution and the number of elements and load increments in the finite element simulations.

## 2 A three-dimensional constitutive model

We use Boyd and Lagoudas [4] and Qidwai and Lagoudas [31]'s three-dimensional phenomenological macroscopic constitutive model for polycrystalline SMAs. In this constitutive model, one starts with the following expression for the total Gibbs free energy $G$:

$$G(\boldsymbol{\sigma}, T, \boldsymbol{\epsilon}^t, \xi) = -\frac{1}{2\rho}\boldsymbol{\sigma} : \mathbb{S} : \boldsymbol{\sigma} - \frac{1}{\rho}\boldsymbol{\sigma} : \left[\boldsymbol{\alpha}\,(T - T_0) + \boldsymbol{\epsilon}^t\right] + c\left[(T - T_0) - T\,\ln\left(\frac{T}{T_0}\right)\right] - s_0 T + u_0 + f(\xi), \tag{1}$$

where, $\mathbb{S}$, $\boldsymbol{\alpha}$, $c$, $\rho$, $s_0$ and $u_0$ are the effective compliance tensor, effective thermal expansion coefficient tensor, effective specific heat, mass density, effective specific entropy, and effective specific internal energy at the reference state, respectively. The symbols $\boldsymbol{\sigma}$, $T$, $T_0$, $\boldsymbol{\epsilon}^t$ and $\xi$ represent the Cauchy stress tensor, temperature, reference temperature, transformation strain, and martensite volume fraction, respectively. All the effective material properties are assumed to vary with the martensitic volume fraction ($\xi$) as follows:

$$\mathbb{S} = \mathbb{S}^A + \xi\Delta\mathbb{S}, \quad \boldsymbol{\alpha} = \boldsymbol{\alpha}^A + \xi\Delta\boldsymbol{\alpha}, \quad c = c^A + \xi\Delta c, \quad s_0 = s_0^A + \xi\Delta s, \quad u_0 = u_0^A + \xi\Delta u_0. \tag{2}$$

The symbol $\Delta(.)$ denotes the difference of a quality $(.)$ between the martensitic and austenitic phases, i.e. $\Delta(.) = (.)^M - (.)^A$, where the superscripts $A$ and $M$ represent the austenite and martensite phases, respectively. In (1), $f(\xi)$ is a hardening function that models the transformation strain hardening in the SMA material. In the Boyd–Lagoudas' polynomial hardening model, this function is given by

$$f(\xi) = \begin{cases} \frac{1}{2}\rho b^M \xi^2 + (\mu_1 + \mu_2)\,\xi, & \dot{\xi} > 0, \\ \frac{1}{2}\rho b^A \xi^2 + (\mu_1 - \mu_2)\,\xi, & \dot{\xi} < 0, \end{cases} \tag{3}$$

where, $\rho b^A$, $\rho b^M$, $\mu_1$ and $\mu_2$ are material constants for transformation strain hardening. The first condition in (3) represents the forward phase transformation ($A \rightarrow M$), and the second condition represents the reverse phase transformation ($M \rightarrow A$). The constitutive relation of a shape memory material can be obtained by using the total Gibbs free energy as

$$\boldsymbol{\epsilon} = -\rho \frac{\partial G}{\partial \boldsymbol{\sigma}} = \mathbb{S} : \boldsymbol{\sigma} + \boldsymbol{\alpha} \left(T - T_0\right) + \boldsymbol{\epsilon}^t. \tag{4}$$

Considering the fact that any change in the state of the system is only possible by a change in the internal state variable $\xi$, the evolution of the transformation strain tensor is related to the evolution of the martensitic volume fraction as [2]

$$\dot{\boldsymbol{\epsilon}}^t = \boldsymbol{\Gamma} \dot{\xi}, \tag{5}$$

where $\boldsymbol{\Gamma}$ represents a transformation tensor related to the deviatoric stress and determines the flow direction as

$$\boldsymbol{\Gamma} = \begin{cases} \frac{3}{2} H \frac{\boldsymbol{\sigma}'}{\overline{\sigma}}, & \dot{\xi} > 0, \\ \\ H \frac{\boldsymbol{\epsilon}^{tr}}{\overline{\epsilon}^{tr}}, & \dot{\xi} < 0. \end{cases} \tag{6}$$

In (6), $H$ is the maximum uniaxial transformation strain and $\boldsymbol{\epsilon}^{tr}$ represents the value of transformation strain at the reverse phase transformation. The terms $\boldsymbol{\sigma}'$, $\overline{\sigma}$ and $\overline{\epsilon}^{tr}$ are the deviatoric stress tensor, the second deviatoric stress invariant, and the second deviatoric transformation strain invariant, respectively, and are expressed as

$$\boldsymbol{\sigma}' = \boldsymbol{\sigma} - \frac{1}{3}(\mathrm{tr}\,\boldsymbol{\sigma})\mathbf{I}, \quad \overline{\sigma} = \sqrt{\frac{3}{2}\boldsymbol{\sigma}' : \boldsymbol{\sigma}'}, \quad \overline{\epsilon}^{tr} = \sqrt{\frac{2}{3}\boldsymbol{\epsilon}^{tr} : \boldsymbol{\epsilon}^{tr}}, \tag{7}$$

where $\mathbf{I}$ is the identity tensor.

An additional constraint on the material behavior is obtained by using the Second Law of Thermodynamics in the form of non-negativeness of the rate of entropy production density [31]:

$$\boldsymbol{\sigma} : \dot{\boldsymbol{\epsilon}}^t - \rho \frac{\partial G}{\partial \xi} \dot{\xi} = \pi \dot{\xi} \geq 0, \tag{8}$$

where $\pi$ is a thermodynamic force and can be obtained by substituting (1) and (5) into (8) as

$$\begin{aligned} \pi = {} & \boldsymbol{\sigma} : \boldsymbol{\Gamma} + \frac{1}{2}\boldsymbol{\sigma} : \Delta\mathbb{S} : \boldsymbol{\sigma} + \Delta\boldsymbol{\alpha} : \boldsymbol{\sigma} \left(T - T_0\right) \\ & -\rho\Delta c \left[ \left(T - T_0\right) - T \ln\left(\frac{T}{T_0}\right) \right] + \rho \Delta s_0 T - \frac{\partial f}{\partial \xi} - \rho \Delta u_0. \end{aligned} \tag{9}$$

Now, the transformation function that controls the onset of direct and reverse phase transformations is defined as

$$\Phi = \begin{cases} \pi - Y, & \dot{\xi} > 0, \\ -\pi - Y, & \dot{\xi} < 0, \end{cases} \tag{10}$$

where $Y$ is a measure of internal dissipation due to microstructural changes during phase transformation.

## 3 Martensitic volume fraction for plane strain and plane stress conditions

A thick-walled SMA cylinder subjected to uniform internal pressure $p$ is considered (see Fig. 1). For a relatively short cylinder with open ends and in the absence of axial loads, plane stress is a good approximation. For long cylinders, cross sections far from the ends are in a plane strain condition. In both cases, the three-dimensional constitutive relations presented in the previous section can be reduced to two-dimensional constitutive equations.

The only non-zero stress components for the axisymmetric plane stress case are $\sigma_r$ and $\sigma_\theta$. In this case, the trace of stress tensor is $\mathrm{tr}\boldsymbol{\sigma} = \sigma_r + \sigma_\theta$. In the plane strain case, the stress component along the axis of the cylinder is denoted by $\sigma_z$, and trace of the stress tensor is $\mathrm{tr}\boldsymbol{\sigma} = \sigma_r + \sigma_\theta + \sigma_z$. It is worth mentioning that in

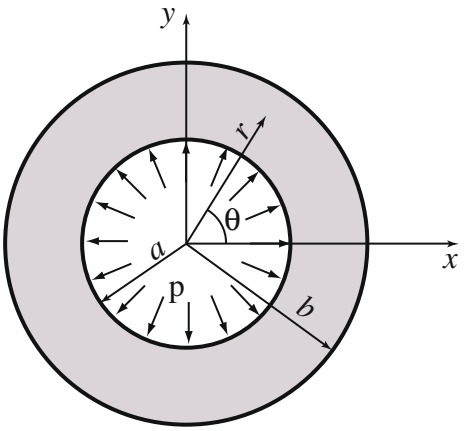


**Fig. 1** Cross section of a thick-walled SMA cylinder subjected to uniform internal pressure

contrast with the classical elasticity problems, the out of plane component of stress cannot be expressed by $\sigma_z = \nu(\sigma_r + \sigma_\theta)$ due to the transformation strain terms. However, for any value of $\sigma_r$ and $\sigma_\theta$, by enforcing the plane strain condition $\epsilon_z = 0$, $\sigma_z$ can be calculated. We will present a brief discussion on calculating $\sigma_z$ for SMAs in plane strain in the sequel. In these special cases (plane stress and plane strain), the deviatoric stress tensor in $(7)_1$ can be rewritten as

$$
\begin{aligned}
{}^{e}\boldsymbol{\sigma}' &= \frac{1}{3}\begin{bmatrix} 2\sigma_r - \sigma_\theta - \sigma_z & 0 & 0 \\ 0 & 2\sigma_\theta - \sigma_r - \sigma_z & 0 \\ 0 & 0 & 2\sigma_z - \sigma_r - \sigma_\theta \end{bmatrix}, \\
{}^{s}\boldsymbol{\sigma}' &= \frac{1}{3}\begin{bmatrix} 2\sigma_r - \sigma_\theta & 0 & 0 \\ 0 & 2\sigma_\theta - \sigma_r & 0 \\ 0 & 0 & -\sigma_r - \sigma_\theta \end{bmatrix},
\end{aligned} \tag{11}
$$

where the left superscripts ${}^{e}(.)$ and ${}^{s}(.)$ represent a parameter in plane strain and plane stress, respectively. This notation will be used throughout the paper. Substituting (11) into $(6)_1$, the transformation tensor for the forward phase transformation can be obtained. By substituting the transformation tensor into (9), the thermodynamic forces for the plane strain and plane stress conditions are obtained as follows:

$$
{}^{e}\pi = H\,{}^{e}\sigma_{\text{eff}} + \frac{1}{2}\Delta S_{11}\,{}^{e}\sigma^{*}_{\text{eff}} + \aleph \quad \text{and} \quad {}^{s}\pi = H\,{}^{s}\sigma_{\text{eff}} + \frac{1}{2}\Delta S_{11}\,{}^{s}\sigma^{*}_{\text{eff}} + \aleph, \tag{12}
$$

where

$$
\begin{aligned}
{}^{e}\sigma_{\text{eff}} &= (\sigma_r^2 + \sigma_\theta^2 + \sigma_z^2 - \sigma_r\sigma_\theta - \sigma_r\sigma_z - \sigma_\theta\sigma_z)^{1/2}, \\
{}^{s}\sigma_{\text{eff}} &= (\sigma_r^2 + \sigma_\theta^2 - \sigma_r\sigma_\theta)^{1/2}, \\
{}^{e}\sigma^{*}_{\text{eff}} &= \left[\sigma_r^2 + \sigma_\theta^2 + \sigma_z^2 - 2\nu(\sigma_r\sigma_\theta + \sigma_r\sigma_z + \sigma_\theta\sigma_z)\right], \\
{}^{s}\sigma^{*}_{\text{eff}} &= (\sigma_r^2 + \sigma_\theta^2 - 2\nu\sigma_r\sigma_\theta), \\
\aleph &= (\Delta\alpha_{11}\sigma_r + \Delta\alpha_{22}\sigma_\theta)(T - T_0) - \rho\,\Delta c\,[(T - T_0) - T\ \ln(T/T_0)] \\
&\quad + \rho\,\Delta s_0 T - \rho b^M \xi - (\mu_1 + \mu_2) - \rho\,\Delta u_0, \\
\Delta S_{11} &= \frac{1}{E^M} - \frac{1}{E^A}.
\end{aligned} \tag{13}
$$

The parameters $E^M$ and $E^A$ represent the elastic moduli for the martensite and austenite phases, respectively, and $\nu$ is the Poisson's ratio, which is assumed to be the same for both phases. Now, (10) and (12) are used in obtaining an explicit expression for the martensitic volume fraction $\xi$. During the forward phase transformation from austenite to martensite ($\dot{\xi} > 0$), the state of stress, temperature and martensitic volume fraction should

remain on the transformation surface characterized by $\Phi = \pi - Y = 0$. By substituting (12) into this condition and using the following relations between the constitutive model parameters:

$$\begin{aligned} \rho\Delta u_0 + \mu_1 &= \frac{1}{2}\rho\Delta s_0(M_s + A_f), \quad \rho b^A = -\rho\Delta s_0(A_f - A_s), \\ \rho b^M &= -\rho\Delta s_0(M_s - M_f), \quad Y = -\frac{1}{2}\rho\Delta s_0(A_f - M_s) - \mu_2, \\ \mu_2 &= \frac{1}{4}\left(\rho b^A - \rho b^M\right), \end{aligned} \tag{14}$$

an explicit expression is obtained for the martensitic volume fraction in plane strain and plain stress states as:

$${}^{e}\xi = \frac{1}{\rho b^M}\left[H\ {}^{e}\sigma_{\text{eff}} + \frac{1}{2}\Delta S_{11}\ {}^{e}\sigma^{*}_{\text{eff}} + f(T) + \widehat{T}\right], \tag{15}$$

$${}^{s}\xi = \frac{1}{\rho b^M}\left[H\ {}^{s}\sigma_{\text{eff}} + \frac{1}{2}\Delta S_{11}\ {}^{s}\sigma^{*}_{\text{eff}} + f(T) + \widehat{T}\right], \tag{16}$$

where

$$f(T) = (\Delta\alpha_{11}\sigma_r + \Delta\alpha_{22}\sigma_\theta)(T - T_0) - \rho\,\Delta c\,[(T - T_0) - T\ \ln(T/T_0)], \quad \widehat{T} = \rho\,\Delta s_0(T - M_s). \tag{17}$$

Transformation surface in the stress-temperature space is represented by two separate faces related to $\xi = 0$ and $\xi = 1$. To obtain the transformation surface in the plane strain case, for each value of the radial and circumferential stresses, the plane strain condition in the reference temperature $T = T_0$ is given by the following algebraic equation (see the constitutive relation in (4))

$$\epsilon_z = D_{eq}(\sigma_r - \nu\sigma_\theta - \nu\sigma_z) + \frac{1}{2}\frac{H}{{}^{e}\sigma_{\text{eff}}}(2\sigma_z - \sigma_r - \sigma_\theta)\ {}^{e}\xi = 0, \tag{18}$$

where $(H/2^{e}\sigma_{\text{eff}})(2\sigma_z - \sigma_r - \sigma_\theta)\ {}^{e}\xi$ is the out of plane transformation strain $\epsilon^t_z$ (calculating the transformation strain components will be explained in more detail in Sect. 4). The martensitic volume fraction is expressed in (15), and the effective compliance component $D_{eq}$ is

$$D_{eq} = \frac{1}{E^A + {}^{e}\xi(E^M - E^A)}. \tag{19}$$

In the plane strain case, for any known $(\sigma_r, \sigma_\theta)$ stress state, (18) is an algebraic equation with $\sigma_z$ as the only unknown. For finding the transformation function, for each value of the circumferential and radial stresses, (18) is solved numerically [9], and $\sigma_z$ is calculated. Having the stress components, (15) and (16) are used to obtain the transformation functions in both plane stress and plane strain cases. At a given temperature, the transformation functions $\xi = 0$ and $\xi = 1$ are represented by curves in $(\sigma_r, \sigma_\theta)$ stress space. Figure 2 shows the transformation function in the start and finish of phase transformation for both the plane stress and plane strain conditions (material properties of Table 1 are used in plotting these curves). For any state of stress inside the $\xi = 0$ region, the material is in the fully austenite phase. The stress points outside $\xi = 1$ represent a fully martensite case, and any stress state between these two surfaces represents the material with phase transformation $0 < \xi < 1$.

As it is shown in Fig. 2, in the plane strain case, the $\xi = 1$ curve is stretched along the $\sigma_r = \sigma_\theta$ line. For studying this phenomenon, the out of plane stress obtained from solving the plane strain condition in (18) for any $(\sigma_r, \sigma_\theta)$ stress sate is plotted in Fig. 3. As it is shown in this figure, for any $(\sigma_r, \sigma_\theta)$ stress state inside the $\xi = 0$ curve (see Fig. 2), the value of $\sigma_z$ is identical with the elastic case ($\sigma_z = \nu(\sigma_r - \sigma_\theta)$). Between the $\xi = 0$ and $\xi = 1$ curves, $\sigma_z$ varies non-linearly and is obtained from solving (18), and for any state of stress outside the $\xi = 1$ curve, the value of $\sigma_z$ is not unique and depends on the loading path[1]. By increase in stresses on the $\sigma_r = \sigma_\theta$ path, the solution of (18) approaches $\sigma_z = \sigma_r = \sigma_\theta$, i.e. the hydrostatic stress state. Note that the presented constitutive relations are based on $J_2$ plasticity, and the transformation function is an open surface along the hydrostatic pressure in this case [31]. That is the reason of having an open curve in Fig. 2 for the plane strain case.

[1] For calculating $\sigma_z$ outside the $\xi = 1$ curve, the plane strain condition $\epsilon_z = \frac{1}{E_M}(\sigma_r - \nu\sigma_\theta - \nu\sigma_z) + \tilde{\epsilon}^t_z = 0$ is solved in which $\tilde{\epsilon}^t_z$ is the final value of axial transformation strain during loading at the point that phase transformation has been completed. We will discuss this case in more detail in Sect. 6.

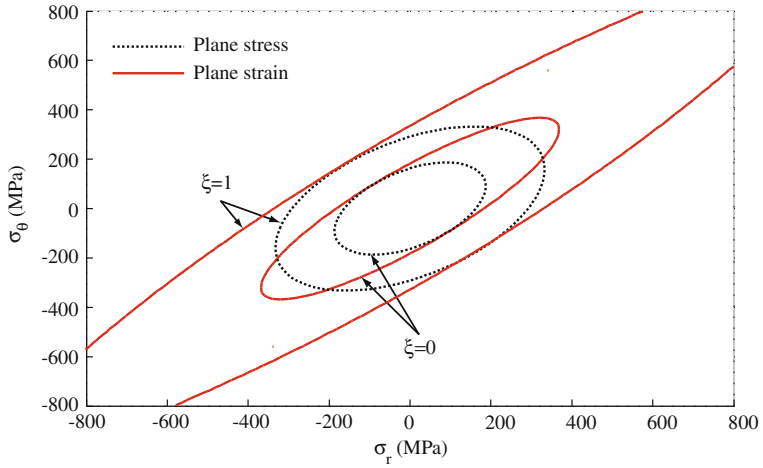


**Fig. 2** Transformation function in $\sigma_r - \sigma_\theta$ space at $T = 315K$ for both plane stress and plane strain cases

**Table 1** SMA material parameters

| Material constants | A generic SMA [32] |
|---|---|
| $E^A$ | $70.0 \times 10^9$Pa |
| $E^M$ | $30.0 \times 10^9$Pa |
| $\nu^A = \nu^M$ | 0.3 |
| $\alpha^A$ | $22.0 \times 10^{-6}$/K |
| $\alpha^{\mathrm{M}}$ | $10.0 \times 10^{-6}$/K |
| $\rho\Delta c = c^M - c^A$ | 0.0 J/(m$^3$K) |
| $H$ | 0.05 |
| $\rho\Delta s_0$ | $-0.35 \times 10^6$J/(m$^3$K) |
| $A_f$ | 315.0 K |
| $A_s$ | 295.0 K |
| $M_s$ | 291.0 K |
| $M_f$ | 271.0 K |

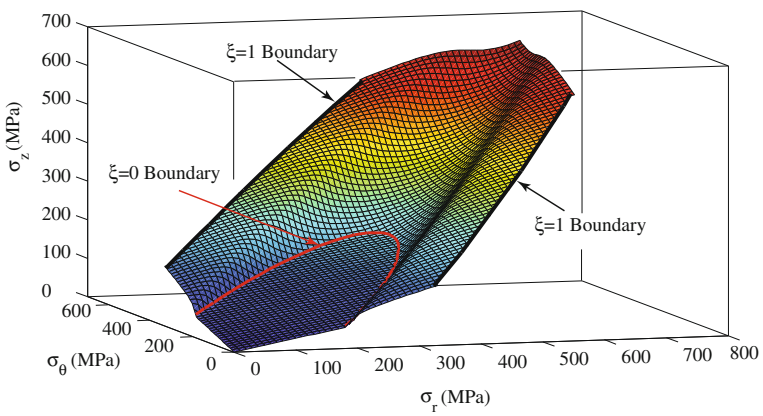


**Fig. 3** $\sigma_z$ in plane strain as a function of $\sigma_r$ and $\sigma_\theta$

The elastic radial and hoop stress distributions for a thick-walled cylinder in plane stress or plane strain (see Fig. 1) can be expressed as [3]:

$$\sigma_r = \frac{pa^2(r^2 - b^2)}{r^2(b^2 - a^2)} \quad \text{and} \quad \sigma_\theta = \frac{pa^2(r^2 + b^2)}{r^2(b^2 - a^2)}. \tag{20}$$

The axial stress component in plane strain for an elastic cylinder is expressed as $\sigma_z = \nu(\sigma_r - \sigma_\theta)$. Considering (15), (16), (20), and using the dimensionless quantities $R = r/a$ and $\beta = b/a$, the following expressions

are obtained for the martensitic volume fraction in plane strain and plane stress as functions of internal pressure (using $\Delta c = \Delta\alpha_{11} = \Delta\alpha_{22} = 0$):

$$
\begin{aligned}
{}^{e}\xi = {} & \frac{H}{\rho b^{M}} \frac{p}{R^2(\beta^2-1)} \sqrt{4\,\nu^2 R^4 - 4\,\nu\, R^4 + 3\,\beta^4 + R^4} \\
& + \frac{\Delta S_{11}}{\rho b^{M}} \frac{p^2}{R^4(1-\beta^2)^2} \left(\beta^4 + R^4 - 2\,\nu^2 R^4 + \nu\beta^4 - \nu R^4\right) + \frac{\widehat{T}}{\rho b^{M}}, \qquad (21) \\
{}^{s}\xi = {} & \frac{H}{\rho b^{M}} \frac{p}{R^2(\beta^2-1)} \sqrt{3\beta^4 + R^4} \\
& + \frac{\Delta S_{11}}{\rho b^{M}} \frac{p^2}{R^4(1-\beta^2)^2} \left(\beta^4 + R^4 + \nu\beta^4 - \nu R^4\right) + \frac{\widehat{T}}{\rho b^{M}}. \qquad (22)
\end{aligned}
$$

In deriving (21) and (22), the elastic stress distribution is considered for the cylinder, so this relation represents an exact expression only for the phase transformation innermost radius at the initiation of phase transformation, which is characterized by $\xi = 0$. Solving (21) and (22) for the parameter $p$ by setting $\xi = 0$ gives:

$$
\begin{aligned}
{}^{e}p = {} & \frac{R_0^2(\beta^2-1)}{2\,\Delta S_{11}(\beta^4 + R_0^4 - 2\,\nu^2 R_0^4 + \nu\beta^4 - \nu R_0^4)} \left( -H\sqrt{4\,\nu^2 R_0^4 - 4\,\nu\, R_0^4 + 3\,\beta^4 + R_0^4} \right. \\
& \left. + \left[ H^2(4\,\nu^2 R_0^4 - 4\,\nu\, R_0^4 + 3\,\beta^4 + R_0^4) - 4\,\widehat{T}\,\Delta S_{11}(\beta^4 + R_0^4 - 2\,\nu^2 R_0^4 + \nu\beta^4 - \nu R_0^4) \right]^{\frac{1}{2}} \right), \qquad (23) \\
{}^{s}p = {} & \frac{R_0^2(\beta^2-1)}{2\,\Delta S_{11}(\beta^4 + R_0^4 + \nu\beta^4 - \nu R_0^4)} \left( -H\sqrt{3\beta^4 + R_0^4} \right. \\
& \left. + \sqrt{3H^2\beta^4 + H^2 R_0^4 - 4\,\widehat{T}\,\Delta S_{11}(\beta^4 + R_0^4 + \nu\beta^4 - \nu R_0^4)} \right). \qquad (24)
\end{aligned}
$$

Since (21) and (22) are solved for $\xi = 0$, we denote the parameter $R$ in this special case by $R_0 = r_0/a$, where $r_0$ is the inner radius of the region in which the phase transformation has not started ($\xi = 0$). Equations (23) and (24) can be used for exact prediction of phase transformation initiation that starts from the inner radius ($R_0 = 1$). Note that in the phase transformation initiation, the whole cylinder is in the austenite phase and the elastic stress distribution in (20) is valid, so (23) and (24) present the exact solution in this case. Figure 4 shows this pressure for different values of $\beta$ and for three different temperatures in both plane stress and plane strain.

As the elastic stress distribution is assumed in deriving (21)–(24), by spread of the regions with phase transformation toward the outer radius, the precision of these relations is reduced as stress distribution in areas with phase transformation is different from the elastic stress distribution. Using (21) and (22), Fig. 5 shows an approximate solution for the spread of phase transformation boundary ($R_0$) as the pressure increases for three different values of temperature. These results are obtained for a thick-walled cylinder with $\beta = 3$ in both plane stress and plane strain. The results of Fig. 5 are exact for $R_0 = 1$ since the phase transformation boundary is at the inner radius in this case and the whole cylinder is in the fully austenite phase with elastic stress distribution. However, when the phase transformation boundary is spread through the outer radius ($R_0 > 1$), the elastic stress distribution is not valid in a portion of the thickness and the results of Fig. 5 are approximate. The exact value for $R_0$ for different internal pressures will be given in the sequel.

## 4 Transformation strains and their derivatives with respect to stress components

In this section, the two-dimensional form of the constitutive relations is expressed for material points with $0 < \xi < 1$. Substituting the transformation tensor into (5) and after integration, the following expressions are obtained for the transformation strain components in plane stress and plane strain:

$$
{}^{e}\epsilon_r^t = \frac{1}{2}\frac{H}{{}^{e}\sigma_{\text{eff}}}(2\sigma_r - \sigma_\theta - \sigma_z)\,\xi, \quad {}^{e}\epsilon_\theta^t = \frac{1}{2}\frac{H}{{}^{e}\sigma_{\text{eff}}}(2\sigma_\theta - \sigma_r - \sigma_z)\,\xi, \quad {}^{e}\epsilon_z^t = \frac{1}{2}\frac{H}{{}^{e}\sigma_{\text{eff}}}(2\sigma_z - \sigma_r - \sigma_\theta)\,\xi, \qquad (25)
$$

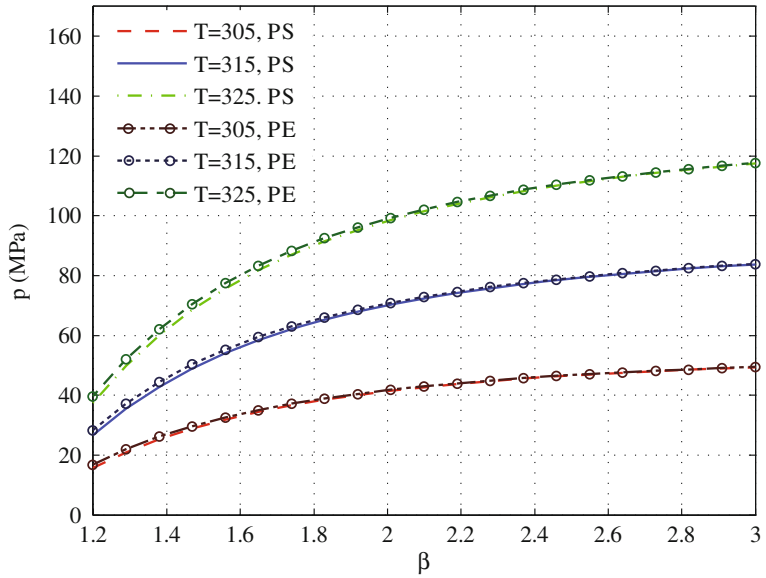


**Fig. 4** Exact value for the minimum pressure required for phase transformation initiation in SMA thick-walled cylinders in both plane stress (PS) and plane strain (PE)

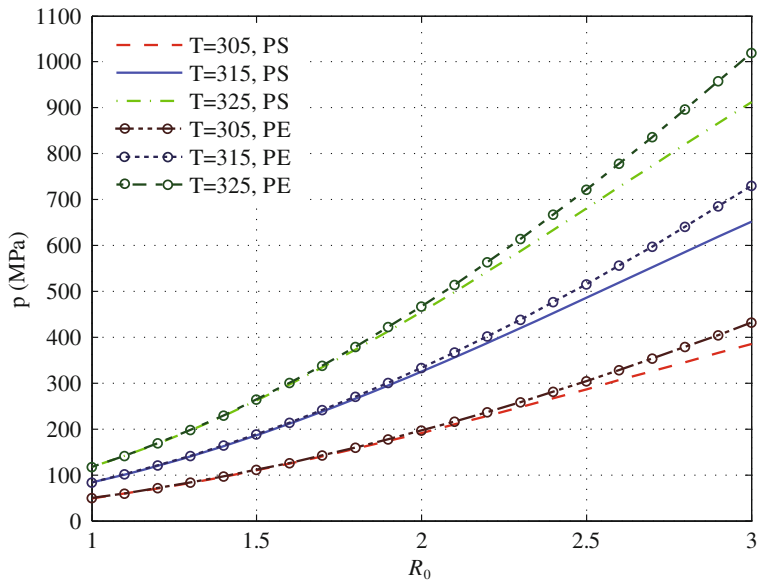


**Fig. 5** An approximate value for the spread of phase transformation boundary in SMA thick-walled cylinders in both plane stress (PS) and plane strain (PE)

and

$$ {}^{s}\epsilon_r^t = \frac{1}{2}\frac{H}{{}^{s}\sigma_{\text{eff}}}(2\sigma_r - \sigma_\theta)\xi, \quad {}^{s}\epsilon_\theta^t = \frac{1}{2}\frac{H}{{}^{s}\sigma_{\text{eff}}}(2\sigma_\theta - \sigma_r)\xi, \tag{26} $$

with the effective stresses expressed in (13). Using $\Delta c = \Delta\alpha_{11} = \Delta\alpha_{22} = 0$, substituting (15) into (25) leads to the following expression for the transformation strain components for the plane stress case:

$$ {}^{s}\epsilon_r^t = {}^{s}\mathscr{F}\,(2\sigma_r - \sigma_\theta), \quad {}^{s}\epsilon_\theta^t = {}^{s}\mathscr{F}\,(2\sigma_\theta - \sigma_r), \tag{27} $$

and the transformation strain components in the plane strain case are obtained by substituting (16) into (26) as:

$$ {}^{e}\epsilon_r^t = {}^{e}\mathscr{F}\,(2\sigma_r - \sigma_\theta - \sigma_z), \quad {}^{e}\epsilon_\theta^t = {}^{e}\mathscr{F}\,(2\sigma_\theta - \sigma_r - \sigma_z), \quad {}^{e}\epsilon_z^t = {}^{e}\mathscr{F}\,(2\sigma_z - \sigma_r - \sigma_\theta), \tag{28} $$

where

$$ {}^{s}\mathscr{F} = \left( \frac{H^2}{2\rho b^M} + \frac{H\Delta S_{11}}{4\rho b^M} \frac{{}^{s}\sigma^{*}_{\text{eff}}}{{}^{s}\sigma_{\text{eff}}} + \frac{H\ \widehat{T}}{2\rho b^M} \frac{1}{{}^{s}\sigma_{\text{eff}}} \right), \quad {}^{e}\mathscr{F} = \left( \frac{H^2}{2\rho b^M} + \frac{H\Delta S_{11}}{4\rho b^M} \frac{{}^{e}\sigma^{*}_{\text{eff}}}{{}^{e}\sigma_{\text{eff}}} + \frac{H\ \widehat{T}}{2\rho b^M} \frac{1}{{}^{e}\sigma_{\text{eff}}} \right). \tag{29} $$

Differentials of transformation strains in (27) and (28), after some lengthy algebraic manipulations, can be written as

$$ \begin{aligned} d({}^{e}\epsilon^{t}_{r}) = \frac{1}{2\rho b^M} \Bigg\{ & \left[ 2H^2 + H\ {}^{e}\mathcal{G} + 2\frac{H\ \widehat{T}}{{}^{e}\sigma_{\text{eff}}} + \left( \frac{1}{2} H\ {}^{e}\mathcal{A} - \frac{H\ \widehat{T}\ {}^{e}\mathcal{M}}{({}^{e}\sigma_{\text{eff}})^2} \right) (2\sigma_r - \sigma_\theta - \sigma_z) \right] d\sigma_r \\ & + \left[ -H^2 - \frac{1}{2} H\ {}^{e}\mathcal{G} - \frac{H\ \widehat{T}}{{}^{e}\sigma_{\text{eff}}} + \left( \frac{1}{2} H\ {}^{e}\mathcal{B} - \frac{H\ \widehat{T}\ {}^{e}\mathcal{N}}{({}^{e}\sigma_{\text{eff}})^2} \right) (2\sigma_r - \sigma_\theta - \sigma_z) \right] d\sigma_\theta \\ & + \left[ -H^2 - \frac{1}{2} H\ {}^{e}\mathcal{G} - \frac{H\ \widehat{T}}{{}^{e}\sigma_{\text{eff}}} + \left( \frac{1}{2} H\ {}^{e}\mathcal{C} - \frac{H\ \widehat{T}\ {}^{e}\mathcal{O}}{({}^{e}\sigma_{\text{eff}})^2} \right) (2\sigma_r - \sigma_\theta - \sigma_z) \right] d\sigma_z \Bigg\}, \end{aligned} \tag{30} $$

$$ \begin{aligned} d({}^{e}\epsilon^{t}_{\theta}) = \frac{1}{2\rho b^M} \Bigg\{ & \left[ -H^2 - \frac{1}{2} H\ {}^{e}\mathcal{G} - \frac{H\ \widehat{T}}{{}^{e}\sigma_{\text{eff}}} + \left( \frac{1}{2} H\ {}^{e}\mathcal{A} - \frac{H\ \widehat{T}\ {}^{e}\mathcal{M}}{({}^{e}\sigma_{\text{eff}})^2} \right) (2\sigma_\theta - \sigma_r - \sigma_z) \right] d\sigma_r \\ & + \left[ 2H^2 + H\ {}^{e}\mathcal{G} + 2\frac{H\ \widehat{T}}{{}^{e}\sigma_{\text{eff}}} + \left( \frac{1}{2} H\ {}^{e}\mathcal{B} - \frac{H\ \widehat{T}\ {}^{e}\mathcal{N}}{({}^{e}\sigma_{\text{eff}})^2} \right) (2\sigma_\theta - \sigma_r - \sigma_z) \right] d\sigma_\theta \\ & + \left[ -H^2 - \frac{1}{2} H\ {}^{e}\mathcal{G} - \frac{H\ \widehat{T}}{{}^{e}\sigma_{\text{eff}}} + \left( \frac{1}{2} H\ {}^{e}\mathcal{C} - \frac{H\ \widehat{T}\ {}^{e}\mathcal{O}}{({}^{e}\sigma_{\text{eff}})^2} \right) (2\sigma_\theta - \sigma_r - \sigma_z) \right] d\sigma_z \Bigg\}, \end{aligned} \tag{31} $$

$$ \begin{aligned} d({}^{e}\epsilon^{t}_{z}) = \frac{1}{2\rho b^M} \Bigg\{ & \left[ -H^2 - \frac{1}{2} H\ {}^{e}\mathcal{G} - \frac{H\ \widehat{T}}{{}^{e}\sigma_{\text{eff}}} + \left( \frac{1}{2} H\ {}^{e}\mathcal{A} - \frac{H\ \widehat{T}\ {}^{e}\mathcal{M}}{({}^{e}\sigma_{\text{eff}})^2} \right) (2\sigma_z - \sigma_r - \sigma_\theta) \right] d\sigma_r \\ & + \left[ -H^2 - \frac{1}{2} H\ {}^{e}\mathcal{G} - \frac{H\ \widehat{T}}{{}^{e}\sigma_{\text{eff}}} + \left( \frac{1}{2} H\ {}^{e}\mathcal{B} - \frac{H\ \widehat{T}\ {}^{e}\mathcal{N}}{({}^{e}\sigma_{\text{eff}})^2} \right) (2\sigma_z - \sigma_r - \sigma_\theta) \right] d\sigma_\theta \\ & + \left[ 2H^2 + H\ {}^{e}\mathcal{G} + 2\frac{H\ \widehat{T}}{{}^{e}\sigma_{\text{eff}}} + \left( \frac{1}{2} H\ {}^{e}\mathcal{C} - \frac{H\ \widehat{T}\ {}^{e}\mathcal{O}}{({}^{e}\sigma_{\text{eff}})^2} \right) (2\sigma_z - \sigma_r - \sigma_\theta) \right] d\sigma_z \Bigg\}, \end{aligned} \tag{32} $$

for plane strain and

$$ \begin{aligned} d({}^{s}\epsilon^{t}_{r}) = \frac{1}{2\rho b^M} \Bigg\{ & \left[ 2H^2 + H\ {}^{s}\mathcal{G} + 2\frac{H\ \widehat{T}}{{}^{s}\sigma_{\text{eff}}} + \left( \frac{1}{2} H\ {}^{s}\mathcal{A} - \frac{H\ \widehat{T}\ {}^{s}\mathcal{M}}{({}^{s}\sigma_{\text{eff}})^2} \right) (2\sigma_r - \sigma_\theta) \right] d\sigma_r \\ & + \left[ -H^2 - \frac{1}{2} H\ {}^{s}\mathcal{G} - \frac{H\ \widehat{T}}{{}^{s}\sigma_{\text{eff}}} + \left( \frac{1}{2} H\ {}^{s}\mathcal{B} - \frac{H\ \widehat{T}\ {}^{s}\mathcal{N}}{({}^{s}\sigma_{\text{eff}})^2} \right) (2\sigma_r - \sigma_\theta) \right] d\sigma_\theta \Bigg\}, \end{aligned} \tag{33} $$

$$ \begin{aligned} d({}^{s}\epsilon^{t}_{\theta}) = \frac{1}{2\rho b^M} \Bigg\{ & \left[ -H^2 - \frac{1}{2} H\ {}^{s}\mathcal{G} - \frac{H\ \widehat{T}}{{}^{s}\sigma_{\text{eff}}} + \left( \frac{1}{2} H\ {}^{s}\mathcal{A} - \frac{H\ \widehat{T}\ {}^{s}\mathcal{M}}{({}^{s}\sigma_{\text{eff}})^2} \right) (2\sigma_\theta - \sigma_r) \right] d\sigma_r \\ & + \left[ 2H^2 + H\ {}^{s}\mathcal{G} + 2\frac{H\ \widehat{T}}{{}^{s}\sigma_{\text{eff}}} + \left( \frac{1}{2} H\ {}^{s}\mathcal{B} - \frac{H\ \widehat{T}\ {}^{s}\mathcal{N}}{({}^{s}\sigma_{\text{eff}})^2} \right) (2\sigma_\theta - \sigma_r) \right] d\sigma_\theta \Bigg\}, \end{aligned} \tag{34} $$

for plane stress, where

$$
\begin{aligned}
{}^{e}\mathcal{M} &= \frac{2\sigma_r - \sigma_\theta - \sigma_z}{2\,{}^{e}\sigma_{\text{eff}}}, {}^{e}\mathcal{N} = \frac{2\sigma_\theta - \sigma_r - \sigma_z}{2\,{}^{e}\sigma_{\text{eff}}}, \quad {}^{e}\mathcal{O} = \frac{2\sigma_z - \sigma_r - \sigma_\theta}{2\,{}^{e}\sigma_{\text{eff}}},\\
{}^{e}\mathcal{A} &= \frac{\Delta S_{11}}{({}^{e}\sigma_{\text{eff}})^2}\left[{}^{e}\sigma_{\text{eff}}\,(2\sigma_r - 2\nu\sigma_\theta - 2\nu\sigma_z) - {}^{e}\mathcal{M}\,{}^{e}\sigma^{*}_{\text{eff}}\right],\\
{}^{e}\mathcal{B} &= \frac{\Delta S_{11}}{({}^{e}\sigma_{\text{eff}})^2}\left[{}^{e}\sigma_{\text{eff}}\,(2\sigma_\theta - 2\nu\sigma_r - 2\nu\sigma_z) - {}^{e}\mathcal{N}\,{}^{e}\sigma^{*}_{\text{eff}}\right],\\
{}^{e}\mathcal{C} &= \frac{\Delta S_{11}}{({}^{e}\sigma_{\text{eff}})^2}\left[{}^{e}\sigma_{\text{eff}}\,(2\sigma_z - 2\nu\sigma_r - 2\nu\sigma_\theta) - {}^{e}\mathcal{O}\,{}^{e}\sigma^{*}_{\text{eff}}\right],\\
{}^{s}\mathcal{M} &= \frac{2\sigma_r - \sigma_\theta}{2\,{}^{s}\sigma_{\text{eff}}}, {}^{s}\mathcal{N} = \frac{2\sigma_\theta - \sigma_r}{2\,{}^{s}\sigma_{\text{eff}}},\\
{}^{s}\mathcal{A} &= \frac{\Delta S_{11}}{({}^{s}\sigma_{\text{eff}})^2}\left[{}^{s}\sigma_{\text{eff}}\,(2\sigma_r - 2\nu\sigma_\theta) - {}^{s}\mathcal{M}\,{}^{s}\sigma^{*}_{\text{eff}}\right], {}^{s}\mathcal{B} = \frac{\Delta S_{11}}{({}^{s}\sigma_{\text{eff}})^2}\left[{}^{s}\sigma_{\text{eff}}\,(2\sigma_\theta - 2\nu\sigma_r) - {}^{s}\mathcal{N}\,{}^{s}\sigma^{*}_{\text{eff}}\right],\\
{}^{e}\mathcal{G} &= \Delta S_{11}\,\frac{{}^{e}\sigma^{*}_{\text{eff}}}{{}^{e}\sigma_{\text{eff}}}, {}^{s}\mathcal{G} = \Delta S_{11}\,\frac{{}^{s}\sigma^{*}_{\text{eff}}}{{}^{s}\sigma_{\text{eff}}}.
\end{aligned}
\tag{35}
$$

On the other hand by considering the fact that the transformation strains (in both plane stress and plane strain) are functions of material constants and the stress components, their differentials can be expressed as

$$
\begin{aligned}
d({}^{e}\epsilon^{t}_{r}) &= \frac{\partial({}^{e}\epsilon^{t}_{r})}{\partial\sigma_r}d\sigma_r + \frac{\partial({}^{e}\epsilon^{t}_{r})}{\partial\sigma_\theta}d\sigma_\theta + \frac{\partial({}^{e}\epsilon^{t}_{r})}{\partial\sigma_z}d\sigma_z, \quad d({}^{e}\epsilon^{t}_{\theta}) = \frac{\partial({}^{e}\epsilon^{t}_{\theta})}{\partial\sigma_r}d\sigma_r + \frac{\partial({}^{e}\epsilon^{t}_{\theta})}{\partial\sigma_\theta}d\sigma_\theta + \frac{\partial({}^{e}\epsilon^{t}_{\theta})}{\partial\sigma_z}d\sigma_z,\\
d({}^{e}\epsilon^{t}_{z}) &= \frac{\partial({}^{e}\epsilon^{t}_{z})}{\partial\sigma_r}d\sigma_r + \frac{\partial({}^{e}\epsilon^{t}_{z})}{\partial\sigma_\theta}d\sigma_\theta + \frac{\partial({}^{e}\epsilon^{t}_{z})}{\partial\sigma_z}d\sigma_z,
\end{aligned}
\tag{36}
$$

and

$$
d({}^{s}\epsilon^{t}_{r}) = \frac{\partial({}^{s}\epsilon^{t}_{r})}{\partial\sigma_r}d\sigma_r + \frac{\partial({}^{s}\epsilon^{t}_{r})}{\partial\sigma_\theta}d\sigma_\theta, \quad d({}^{s}\epsilon^{t}_{\theta}) = \frac{\partial({}^{s}\epsilon^{t}_{\theta})}{\partial\sigma_r}d\sigma_r + \frac{\partial({}^{s}\epsilon^{t}_{\theta})}{\partial\sigma_\theta}d\sigma_\theta. \tag{37}
$$

Now, comparing (30)–(32) with (36) and (33)–(34) with (37) term by term, the derivatives of transformation strain components with respect to stress components can be obtained. Note that the expressions in (27) and (28) are valid only in regions that contain both austenite and martensite ($0 < \xi < 1$). In the following sections, the constitutive equations are linearized using the calculated derivatives of transformation strain components. The closed-form solutions are considered for two different cases. We will present the linearized constitutive equations for the regions with partial phase transformation ($0 < \xi < 1$) in Sect. 5. The constitutive equation of Sect. 5 is applicable for the whole cylinder when the material in the inner radius is not completely transformed to martensite. The linearized constitutive relations for regions fully transformed to martensite ($\xi = 1$) are given in Sect. 6. When the martensitic volume fraction reaches the value $\xi = 1$ at the inner radius, increase in pressure will cause the extension of martensite region toward the outer radius and the constitutive relations of Sect. 6 should be considered in analyzing regions that are fully transferred to martensite.

## 5 Semi-analytic solutions when the inner radius is not completely transformed to martensite

As was shown in Sect. 3, for a thick-walled cylinder subjected to internal pressure, the phase transformation initiates from the inner radius and spreads toward the outer radius for both plane stress and plane strain. So, it can be concluded that when the inner radius is not completely converted to martensite, throughout the thickness, the transformation strains can be expressed by (27) and (28) for the regions in which $0 < \xi < 1$ and they would be zero in the regions in which phase transformation has not started yet.

The solution in this case is obtained by splitting the applied pressure into a finite number of increments. By assuming that the solution is known in the $n$th increment[2] and by considering the derivatives of the transformation strain with respect to the stress components, linearized constitutive relations are used for finding

[2] Zero internal pressure can be considered for the first increment. However, it is more efficient to consider a pressure for which the whole cylinder is in the austenite phase as the first increment. The value of the pressure that causes phase transformation to start was calculated in (23) and (24).

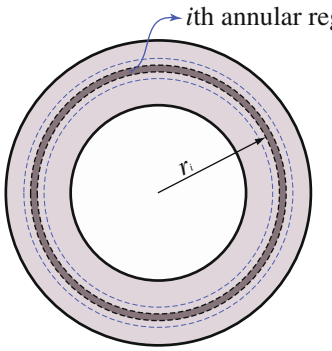


**Fig. 6** Partitioning the cylinder's cross section into a finite number of narrow annular regions

the solution in the $(n+1)$th increment. The transformation strains in the $i$th annular region for the $(n+1)$th increment of loading can be expressed as:

$$ {}^{n+1}\left({}^{e}\epsilon_r^t\right)^i = {}^{n}\left(\frac{\partial\, {}^{e}\epsilon_r^t}{\partial\sigma_r}\right)^i \left({}^{n+1}\sigma_r^i - {}^{n}\sigma_r^i\right) + {}^{n}\left(\frac{\partial\, {}^{e}\epsilon_r^t}{\partial\sigma_\theta}\right)^i \left({}^{n+1}\sigma_\theta^i - {}^{n}\sigma_\theta^i\right) + {}^{n}\left(\frac{\partial\, {}^{e}\epsilon_r^t}{\partial\sigma_z}\right)^i \left({}^{n+1}\sigma_z^i - {}^{n}\sigma_z^i\right) + {}^{n}({}^{e}\epsilon_r^t)^i, \tag{38} $$

$$ {}^{n+1}({}^{e}\epsilon_\theta^t)^i = {}^{n}\left(\frac{\partial\, {}^{e}\epsilon_\theta^t}{\partial\sigma_r}\right)^i \left({}^{n+1}\sigma_r^i - {}^{n}\sigma_r^i\right) + {}^{n}\left(\frac{\partial\, {}^{e}\epsilon_\theta^t}{\partial\sigma_\theta}\right)^i \left({}^{n+1}\sigma_\theta^i - {}^{n}\sigma_\theta^i\right) + {}^{n}\left(\frac{\partial\, {}^{e}\epsilon_\theta^t}{\partial\sigma_z}\right)^i \left({}^{n+1}\sigma_z^i - {}^{n}\sigma_z^i\right) + {}^{n}({}^{e}\epsilon_\theta^t)^i, \tag{39} $$

$$ {}^{n+1}({}^{e}\epsilon_z^t)^i = {}^{n}\left(\frac{\partial\, {}^{e}\epsilon_z^t}{\partial\sigma_r}\right)^i \left({}^{n+1}\sigma_r^i - {}^{n}\sigma_r^i\right) + {}^{n}\left(\frac{\partial\, {}^{e}\epsilon_z^t}{\partial\sigma_\theta}\right)^i \left({}^{n+1}\sigma_\theta^i - {}^{n}\sigma_\theta^i\right) + {}^{n}\left(\frac{\partial\, {}^{e}\epsilon_z^t}{\partial\sigma_z}\right)^i \left({}^{n+1}\sigma_z^i - {}^{n}\sigma_z^i\right) + {}^{n}({}^{e}\epsilon_z^t)^i, \tag{40} $$

for plane strain and

$$ {}^{n+1}({}^{s}\epsilon_r^t)^i = {}^{n}\left(\frac{\partial\, {}^{s}\epsilon_r^t}{\partial\sigma_r}\right)^i \left({}^{n+1}\sigma_r^i - {}^{n}\sigma_r^i\right) + {}^{n}\left(\frac{\partial\, {}^{s}\epsilon_r^t}{\partial\sigma_\theta}\right)^i \left({}^{n+1}\sigma_\theta^i - {}^{n}\sigma_\theta^i\right) + {}^{n}({}^{s}\epsilon_r^t)^i, \tag{41} $$

$$ {}^{n+1}({}^{s}\epsilon_\theta^t)^i = {}^{n}\left(\frac{\partial\, {}^{s}\epsilon_\theta^t}{\partial\sigma_r}\right)^i \left({}^{n+1}\sigma_r^i - {}^{n}\sigma_r^i\right) + {}^{n}\left(\frac{\partial\, {}^{s}\epsilon_\theta^t}{\partial\sigma_\theta}\right)^i \left({}^{n+1}\sigma_\theta^i - {}^{n}\sigma_\theta^i\right) + {}^{n}({}^{s}\epsilon_\theta^t)^i, \tag{42} $$

for plane stress. In deriving (38)–(42), continuous functions of transformation strain derivatives are replaced by piece-wise constant functions. The cylinder is divided into a finite number of narrow annular regions as shown in Fig. 6. The transformation strain derivatives are assumed constant in each region. Increasing the number of annular regions, the accuracy of this method increases.

By applying the load incrementally, the stress components, transformation strain components, and the transformation strain derivatives are known in the $n$th increment. We start from a load value for which the whole cylinder is in the austenite phase. In this case, the stress components for the first increment are calculated from the elastic solution. Increasing the internal pressure incrementally, the start of phase transformation is checked in each annular region by calculating the martensitic volume fraction using (15) and (16). For each annular region, the phase transformation starts at a specific load increment. For this special increment, Eqs. (38)–(42) should be considered with a minor modification. Figure 7 shows the circumferential transformation strain surface in the stress space for plane stress. At the start of phase transformation in an annular region, the $(n+1)$th stress state corresponds to a generic point $B$ that lies between $\xi = 0$ and $\xi = 1$ curves (see Fig. 2 and note that a part of these curves is shown in Fig. 7), while the stress state in the $n$th increment lies inside the $\xi = 0$ curve (point $A$ in Fig. 7). For this increment, neither the elastic solution nor the solution presented in (41) and (42) can be used as in deriving these equations it is assumed that the stress state in the $n$th increment corresponds to a point on the transformation strain surface located between $\xi = 0$ and $\xi = 1$ curves. However, these relations can be used for this special increment with the following minor modification. The loading path between the stress states $A$ and $B$ is assumed linear as shown in Fig. 7. The intersection of this line with $\xi = 0$ curve is found numerically (point $k$ in Fig. 7), and the stress components corresponding to

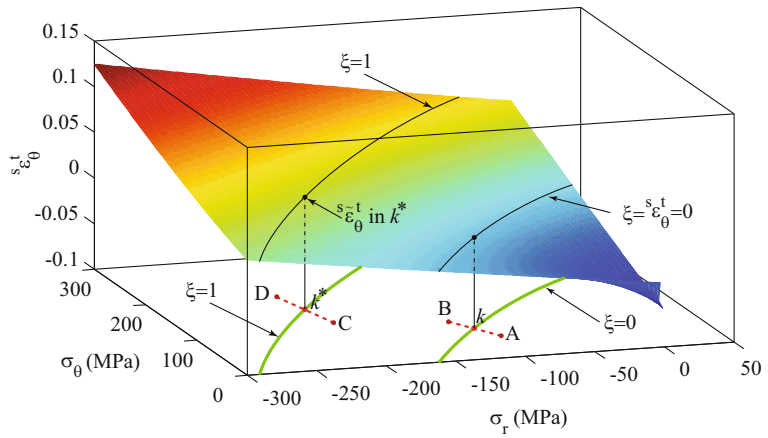


**Fig. 7** Method of calculating the circumferential transformation strain for the special increments in which phase transformation starts and completes in the plane stress case

this point are used instead of ${}^{n}\sigma_r^i$ and ${}^{n}\sigma_\theta^i$ in (41) and (42). It is obvious that the parameters ${}^{n}({}^{s}\epsilon_r^t)^i$ and ${}^{n}({}^{s}\epsilon_\theta^t)^i$ are zero for this increment since $\xi = 0$ at $k$ (see (25) and (26)). In the plane strain case, the same procedure is used for finding the circumferential and radial stress components at the onset of phase transformation in each region. The axial stress component is calculated by ${}^{n}\sigma_z^i = \nu({}^{n}\sigma_r^i + {}^{n}\sigma_\theta^i)$ (see the plane strain condition in (18) with ${}^{e}\xi = 0$).

The total strain components for the $i$th annular region at the $(n+1)$th load increment can be expressed as:

$$\begin{aligned}
{}^{n+1}({}^{e}\epsilon_r)^i &= {}^{n}S_{11}^i\ {}^{n+1}\sigma_r^i + {}^{n}S_{12}^i\ {}^{n+1}\sigma_\theta^i + {}^{n}S_{13}^i\ {}^{n+1}\sigma_z^i + {}^{n}d_1^i,\\
{}^{n+1}({}^{e}\epsilon_\theta)^i &= {}^{n}S_{21}^i\ {}^{n+1}\sigma_r^i + {}^{n}S_{22}^i\ {}^{n+1}\sigma_\theta^i + {}^{n}S_{23}^i\ {}^{n+1}\sigma_z^i + {}^{n}d_2^i,\\
0 &= {}^{n}S_{31}^i\ {}^{n+1}\sigma_r^i + {}^{n}S_{32}^i\ {}^{n+1}\sigma_\theta^i + {}^{n}S_{33}^i\ {}^{n+1}\sigma_z^i + {}^{n}d_3^i,
\end{aligned} \tag{43}$$

in plane strain and

$${}^{n+1}({}^{s}\epsilon_r)^i = {}^{n}S_{11}^i\ {}^{n+1}\sigma_r^i + {}^{n}S_{12}^i\ {}^{n+1}\sigma_\theta^i + {}^{n}d_1^i, \quad {}^{n+1}({}^{s}\epsilon_\theta)^i = {}^{n}S_{21}^i\ {}^{n+1}\sigma_r^i + {}^{n}S_{22}^i\ {}^{n+1}\sigma_\theta^i + {}^{n}d_2^i, \tag{44}$$

in plane stress. The parameters $S$ and $d$ in (43) for the plane strain are expressed as

$$\begin{aligned}
{}^{n}S_{11}^i &= {}^{n}D_{eq}^i + {}^{n}\left(\frac{\partial\ {}^{e}\epsilon_r^t}{\partial\sigma_r}\right)^i, \quad {}^{n}S_{12}^i = -\nu\ {}^{n}D_{eq}^i + {}^{n}\left(\frac{\partial\ {}^{e}\epsilon_r^t}{\partial\sigma_\theta}\right)^i, \quad {}^{n}S_{13}^i = -\nu\ {}^{n}D_{eq}^i + {}^{n}\left(\frac{\partial\ {}^{e}\epsilon_r^t}{\partial\sigma_z}\right)^i,\\
{}^{n}S_{21}^i &= -\nu\ {}^{n}D_{eq}^i + {}^{n}\left(\frac{\partial\ {}^{e}\epsilon_\theta^t}{\partial\sigma_r}\right)^i, \quad {}^{n}S_{22}^i = {}^{n}D_{eq}^i + {}^{n}\left(\frac{\partial\ {}^{e}\epsilon_\theta^t}{\partial\sigma_\theta}\right)^i, \quad {}^{n}S_{23}^i = -\nu\ {}^{n}D_{eq}^i + {}^{n}\left(\frac{\partial\ {}^{e}\epsilon_\theta^t}{\partial\sigma_z}\right)^i,\\
{}^{n}S_{31}^i &= -\nu\ {}^{n}D_{eq}^i + {}^{n}\left(\frac{\partial\ {}^{e}\epsilon_z^t}{\partial\sigma_r}\right)^i, \quad {}^{n}S_{32}^i = -\nu\ {}^{n}D_{eq}^i + {}^{n}\left(\frac{\partial\ {}^{e}\epsilon_z^t}{\partial\sigma_\theta}\right)^i, \quad {}^{n}S_{33}^i = {}^{n}D_{eq}^i + {}^{n}\left(\frac{\partial\ {}^{e}\epsilon_z^t}{\partial\sigma_z}\right)^i,\\
{}^{n}d_1^i &= -{}^{n}\left(\frac{\partial\ {}^{e}\epsilon_r^t}{\partial\sigma_r}\right)^i {}^{n}\sigma_r^i - {}^{n}\left(\frac{\partial\ {}^{e}\epsilon_r^t}{\partial\sigma_\theta}\right)^i {}^{n}\sigma_\theta^i - {}^{n}\left(\frac{\partial\ {}^{e}\epsilon_r^t}{\partial\sigma_z}\right)^i {}^{n}\sigma_z^i + {}^{n}({}^{e}\epsilon_r^t)^i,\\
{}^{n}d_2^i &= -{}^{n}\left(\frac{\partial\ {}^{e}\epsilon_\theta^t}{\partial\sigma_r}\right)^i {}^{n}\sigma_r^i - {}^{n}\left(\frac{\partial\ {}^{e}\epsilon_\theta^t}{\partial\sigma_\theta}\right)^i {}^{n}\sigma_\theta^i - {}^{n}\left(\frac{\partial\ {}^{e}\epsilon_\theta^t}{\partial\sigma_z}\right)^i {}^{n}\sigma_z^i + {}^{n}({}^{e}\epsilon_\theta^t)^i,\\
{}^{n}d_3^i &= -{}^{n}\left(\frac{\partial\ {}^{e}\epsilon_z^t}{\partial\sigma_r}\right)^i {}^{n}\sigma_r^i - {}^{n}\left(\frac{\partial\ {}^{e}\epsilon_z^t}{\partial\sigma_\theta}\right)^i {}^{n}\sigma_\theta^i - {}^{n}\left(\frac{\partial\ {}^{e}\epsilon_z^t}{\partial\sigma_z}\right)^i {}^{n}\sigma_z^i + {}^{n}({}^{e}\epsilon_z^t)^i,\\
{}^{n}D_{eq}^i &= \frac{1}{E^A + {}^{n}\xi^i(E^M - E^A)}.
\end{aligned} \tag{45}$$

For the plane stress case in (44), these parameters should be replaced by

$$
\begin{aligned}
&{}^{n}S^{i}_{11} = {}^{n}D^{i}_{eq} + {}^{n}\left(\frac{\partial\, {}^{s}\epsilon^{t}_{r}}{\partial\sigma_r}\right)^{i}, \quad {}^{n}S^{i}_{12} = -\nu\, {}^{n}D^{i}_{eq} + {}^{n}\left(\frac{\partial\, {}^{s}\epsilon^{t}_{r}}{\partial\sigma_\theta}\right)^{i},\\
&{}^{n}S^{i}_{21} = -\nu\, {}^{n}D^{i}_{eq} + {}^{n}\left(\frac{\partial\, {}^{s}\epsilon^{t}_{\theta}}{\partial\sigma_r}\right)^{i}, \quad {}^{n}S^{i}_{22} = {}^{n}D^{i}_{eq} + {}^{n}\left(\frac{\partial\, {}^{s}\epsilon^{t}_{\theta}}{\partial\sigma_\theta}\right)^{i},\\
&{}^{n}d^{i}_{1} = -{}^{n}\left(\frac{\partial\, {}^{s}\epsilon^{t}_{r}}{\partial\sigma_r}\right)^{i} {}^{n}\sigma^{i}_{r} - {}^{n}\left(\frac{\partial\, {}^{s}\epsilon^{t}_{r}}{\partial\sigma_\theta}\right)^{i} {}^{n}\sigma^{i}_{\theta} + {}^{n}({}^{s}\epsilon^{t}_{r})^{i}, \quad {}^{n}d^{i}_{2} = -{}^{n}\left(\frac{\partial\, {}^{s}\epsilon^{t}_{\theta}}{\partial\sigma_r}\right)^{i} {}^{n}\sigma^{i}_{r} - {}^{n}\left(\frac{\partial\, {}^{s}\epsilon^{t}_{\theta}}{\partial\sigma_\theta}\right)^{i} {}^{n}\sigma^{i}_{\theta} + {}^{n}({}^{s}\epsilon^{t}_{\theta})^{i}.
\end{aligned}
\tag{46}
$$

All the coefficients in (45) and (46) are assumed to be known in the $n$th loading increment. Also, all the coefficients are considered constant within each narrow region. By inverting (43) and (44), the stress-strain relations are obtained for the $i$th region at the $(n+1)$th load increment as follows

$$
{}^{n+1}\sigma^{i}_{r} = {}^{n}C^{i}_{11}\, {}^{n+1}(\epsilon_r)^{i} + {}^{n}C^{i}_{12}\, {}^{n+1}(\epsilon_\theta)^{i} + {}^{n}e^{i}_{1} \quad \text{and} \quad {}^{n+1}\sigma^{i}_{\theta} = {}^{n}C^{i}_{21}\, {}^{n+1}(\epsilon_r)^{i} + {}^{n}C^{i}_{22}\, {}^{n+1}(\epsilon_\theta)^{i} + {}^{n}e^{i}_{2}. \tag{47}
$$

Equation (47) is applicable in both plane strain and plane stress cases. For plane strain, the parameters $\epsilon_r$ and $\epsilon_\theta$ are replaced by ${}^{e}\epsilon_r$ and ${}^{e}\epsilon_\theta$, and the coefficients $C_{mn},\ m,n = 1,2,3$ are the components of the inverse of matrix $S$, a $3\times 3$ matrix with components given in (45). The parameters $e_m,\ m = 1,2$ in the plane strain case are expressed by

$$
{}^{n}e^{i}_{1} = -{}^{n}C^{i}_{11}\, {}^{n}d^{i}_{1} - {}^{n}C^{i}_{12}\, {}^{n}d^{i}_{2} - {}^{n}C^{i}_{13}\, {}^{n}d^{i}_{3} \quad \text{and} \quad {}^{n}e^{i}_{2} = -{}^{n}C^{i}_{21}\, {}^{n}d^{i}_{1} - {}^{n}C^{i}_{22}\, {}^{n}d^{i}_{2} - {}^{n}C^{i}_{23}\, {}^{n}d^{i}_{3}, \tag{48}
$$

with the parameters $d_m,\ m = 1,2,3$ given in (45). For plane stress, the parameters $\epsilon_r$ and $\epsilon_\theta$ in (47) are replaced by ${}^{s}\epsilon_r$ and ${}^{s}\epsilon_\theta$, respectively. The coefficients $C_{mn},\ m,n = 1,2$ are the components of the inverse of matrix $S$, a $2\times 2$ matrix with components introduced in (46). The parameters $e_m,\ m = 1,2$ in plane stress are given by

$$
{}^{n}e^{i}_{1} = -{}^{n}C^{i}_{11}\, {}^{n}d^{i}_{1} - {}^{n}C^{i}_{12}\, {}^{n}d^{i}_{2} \quad \text{and} \quad {}^{n}e^{i}_{2} = -{}^{n}C^{i}_{21}\, {}^{n}d^{i}_{1} - {}^{n}C^{i}_{22}\, {}^{n}d^{i}_{2}, \tag{49}
$$

where $d_m,\ m = 1,2$ are given in (46).

In the absence of body forces, the equations of equilibrium for an axisymmetric problem in cylindrical coordinates are reduced to:

$$
\frac{d\sigma_r}{dr} + \frac{\sigma_r - \sigma_\theta}{r} = 0. \tag{50}
$$

Note that $\epsilon_r = \frac{\partial u}{\partial r}$ and $\epsilon_\theta = \frac{u}{r}$, where $u$ represents the radial displacement. Substituting (47) into (50) and considering the strain-displacement relations, the equilibrium equation in terms of radial displacement is obtained as:

$$
\frac{d^2({}^{n+1}u^{i})}{dr^2} + \frac{1}{r}\frac{d({}^{n+1}u^{i})}{dr} - {}^{n}f^{i}\frac{{}^{n+1}u^{i}}{r^2} + {}^{n}g^{i}\frac{1}{r} = 0, \tag{51}
$$

where ${}^{n+1}u^{i}$ is the radial displacement in the $(n+1)$th loading increment in the $i$th annular region and

$$
{}^{n}f^{i} = \frac{{}^{n}C^{i}_{22}}{{}^{n}C^{i}_{11}}, \quad {}^{n}g^{i} = \frac{{}^{n}e^{i}_{1} - {}^{n}e^{i}_{2}}{{}^{n}C^{i}_{11}}. \tag{52}
$$

Considering constant values for the above parameters in each annular region, a closed-form solution can be obtained for (51) as:

$$
{}^{n+1}u^{i}(r) = \begin{cases} {}^{n+1}A^{i}_{1} r^{\sqrt{{}^{n}f^{i}}} + {}^{n+1}A^{i}_{2} r^{-\sqrt{{}^{n}f^{i}}} + \frac{{}^{n}g^{i}}{{}^{n}f^{i}-1} r & {}^{n}f^{i} > 0, \\ {}^{n+1}A^{i}_{1} \sin\left(\sqrt{-{}^{n}f^{i}}\ln r\right) + {}^{n+1}A^{i}_{2} \cos\left(\sqrt{-{}^{n}f^{i}}\ln r\right) + \frac{{}^{n}g^{i}}{{}^{n}f^{i}-1} r & {}^{n}f^{i} < 0, \end{cases} \tag{53}
$$

where ${}^{n+1}A_1^i$ and ${}^{n+1}A_2^i$ are integration constants that should be found in the $(n+1)$th increment of loading. Substituting (53) into the strain-displacement relations and considering (47), the stress components within the $i$th region are obtained. For $(53)_1$, these components are expressed as

$$
\begin{aligned}
{}^{n+1}\sigma_r = {}& {}^{n+1}A_1^i \left[ r^{\sqrt{{}^n f^i}-1} \left( {}^nC_{11}^i \sqrt{{}^n f^i} + {}^nC_{12}^i \right) \right] + {}^{n+1}A_2^i \left[ r^{-\sqrt{{}^n f^i}-1} \left( {}^nC_{12}^i - {}^nC_{11}^i \sqrt{{}^n f^i} \right) \right] \\
& + \left( {}^nC_{11}^i + {}^nC_{12}^i \right) \frac{{}^n g^i}{{}^n f^i - 1} + {}^n e_1^i, \qquad (54) \\
{}^{n+1}\sigma_\theta = {}& {}^{n+1}A_1^i \left[ r^{\sqrt{{}^n f^i}-1} \left( {}^nC_{21}^i \sqrt{{}^n f^i} + {}^nC_{22}^i \right) \right] + {}^{n+1}A_2^i \left[ r^{-\sqrt{{}^n f^i}-1} \left( {}^nC_{22}^i - {}^nC_{21}^i \sqrt{{}^n f^i} \right) \right] \\
& + \left( {}^nC_{21}^i + {}^nC_{22}^i \right) \frac{{}^n g^i}{{}^n f^i - 1} + {}^n e_2^i. \qquad (55)
\end{aligned}
$$

For $(53)_2$ ,the same procedure is followed. The solutions expressed in (53)–(55) are used for the regions in which the martensitic volume fraction is $0 < \xi < 1$. For those regions in which phase transformation has not started and the material is purely austenite, the above solution should be converted to the elastic solution by eliminating the last term in (53) and the last two terms in (54) and (55).

## 6 Closed-form solutions when the inner radius is completely transformed to martensite

For a special value of internal pressure, the inner radius completely transforms to martensite[3]. For pressures lower than this value, the solution proposed in Sect. 5 would be applicable. By increasing the pressure, the fully martensite region will spread toward the outer radius, and the previous solution is not valid in this region. For the $i$th narrow annular region in which the material is fully transformed to martensite in the $(n+1)$th increment, the strain components can be expressed as

$$
\begin{aligned}
{}^{n+1}({}^e\epsilon_r)^i &= S_{11}^M \, {}^{n+1}\sigma_r^i + S_{12}^M \, {}^{n+1}\sigma_\theta^i + S_{13}^M \, {}^{n+1}\sigma_z^i + ({}^e\tilde{\epsilon}_r^t)^i, \\
{}^{n+1}({}^e\epsilon_\theta)^i &= S_{21}^M \, {}^{n+1}\sigma_r^i + S_{22}^M \, {}^{n+1}\sigma_\theta^i + S_{23}^M \, {}^{n+1}\sigma_z^i + ({}^e\tilde{\epsilon}_\theta^t)^i, \\
0 &= S_{31}^M \, {}^{n+1}\sigma_r^i + S_{32}^M \, {}^{n+1}\sigma_\theta^i + S_{33}^M \, {}^{n+1}\sigma_z^i + ({}^e\tilde{\epsilon}_z^t)^i,
\end{aligned} \qquad (56)
$$

for plane strain and

$$
{}^{n+1}({}^s\epsilon_r)^i = S_{11}^M \, {}^{n+1}\sigma_r^i + S_{12}^M \, {}^{n+1}\sigma_\theta^i + ({}^s\tilde{\epsilon}_r^t)^i \quad \text{and} \quad {}^{n+1}({}^s\epsilon_\theta)^i = S_{21}^M \, {}^{n+1}\sigma_r^i + S_{22}^M \, {}^{n+1}\sigma_\theta^i + ({}^s\tilde{\epsilon}_\theta^t)^i, \qquad (57)
$$

for plane stress, where

$$
S_{mn}^M = \begin{cases} \frac{1}{E^M} & \text{for } m = n, \\ -\frac{\nu^M}{E^M} & \text{for } m \neq n. \end{cases} \qquad (58)
$$

In (58), $m, n = 1, 2, 3$ for plane strain and $m, n = 1, 2$ for plane stress. The terms $({}^e\tilde{\epsilon}_r^t)^i$, $({}^e\tilde{\epsilon}_\theta^t)^i$, and $({}^e\tilde{\epsilon}_z^t)^i$ in (56) and $({}^s\tilde{\epsilon}_r^t)^i$ and $({}^s\tilde{\epsilon}_\theta^t)^i$ in (57) represent the final transformation strain components in the $i$th region for the plane stress and plane strain cases, respectively. For calculating these terms, the martensitic volume fraction in each annular region is monitored in all the increments, and the first loading increment in which the $i$th region is fully transformed to martensite is recorded. In this special increment, the stress state for the $n$th loading increment corresponds to a point located between $\xi = 0$ and $\xi = 1$ curves (see Fig. 2). Point $C$ in Fig. 7 shows the stress state of such a point (the material properties of Table 1 and the plane stress condition are used for depicting the circumferential strain surface). The stress state of this annular region in the $(n+1)$th increment corresponds to a point outside the $\xi = 1$ closed curve (point $D$ in Fig. 7). Approximating the load path between these two points by a line, the stress state corresponding to the intersection of line $C$-$D$ and $\xi = 1$ curve (point $k^*$ in Fig. 7) is calculated numerically. For the plane strain case, the stress component $\sigma_z$ at the corresponding point $k^*$ is calculated by enforcing the plane strain condition as expressed in (18). The final

[3] An explicit expression can not be obtained for this pressure. In each load increment, the martensitic volume fraction in all the annular regions is monitored to find the pressure that causes full transformation to martensite in different regions.

transformation strain components are calculated by substituting the stress sate of this point in (25) and (26) for the plane strain and plane stress cases, respectively (the circumferential transformation strain component corresponding to $k^*$ in the plane stress is shown in Fig. 7). The accuracy of the final transformation strains calculated by this method increases by increasing the number of load increments. We will compare the final transformation strains calculated by our method with those of a finite element simulation in a few numerical examples.

Using the inverses of (56) and (57), the stress-strain relations are expressed as:

$$^{n+1}\sigma_r = C_{11}^M\,{}^{n+1}(\epsilon_r)^i + C_{12}^M\,{}^{n+1}(\epsilon_\theta)^i + \tilde{e}_1^i \quad \text{and} \quad {}^{n+1}\sigma_\theta = C_{12}^M\,{}^{n+1}(\epsilon_r)^i + C_{22}^M\,{}^{n+1}(\epsilon_\theta)^i + \tilde{e}_2^i, \tag{59}$$

which are applicable for both plane stress and plane strain. For considering the relation in plane strain, $\epsilon_r$ and $\epsilon_\theta$ are replaced by ${}^e\epsilon_r$ and ${}^e\epsilon_\theta$, respectively. The coefficients $C_{mn}^M,\ m, n = 1, 2, 3$ are the components of the inverse of matrix $S^M$, a $3 \times 3$ matrix with components given in (58). The parameters $\tilde{e}_m,\ m = 1, 2$ in the plane strain case are

$$\tilde{e}_1^i = -C_{11}^M({}^e\tilde{\epsilon}_r^t)^i - C_{12}^M({}^e\tilde{\epsilon}_\theta^t)^i - C_{13}^M({}^e\tilde{\epsilon}_z^t)^i \quad \text{and} \quad \tilde{e}_2^i = -C_{21}^M({}^e\tilde{\epsilon}_r^t)^i - C_{22}^M({}^e\tilde{\epsilon}_\theta^t)^i - C_{23}^M({}^e\tilde{\epsilon}_z^t)^i. \tag{60}$$

For the plane stress case, $\epsilon_r$ and $\epsilon_\theta$ in (59) are replaced by ${}^s\epsilon_r$ and ${}^s\epsilon_\theta$, respectively. The coefficients $C_{mn}^M,\ m, n = 1, 2$ are the components of the inverse of matrix $S^M$, a $2 \times 2$ matrix with components introduced in (58). The parameters $\tilde{e}_m,\ m = 1, 2$ in this case are expressed by

$$\tilde{e}_1^i = -C_{11}^M({}^s\tilde{\epsilon}_r^t)^i - C_{12}^M({}^s\tilde{\epsilon}_\theta^t)^i \quad \text{and} \quad \tilde{e}_2^i = -C_{21}^M({}^s\tilde{\epsilon}_r^t)^i - C_{22}^M({}^s\tilde{\epsilon}_\theta^t)^i. \tag{61}$$

Substituting (59) into (50) and considering the strain-displacement relations, the equilibrium equation in terms of radial displacement in the $i$th region is obtained. Using assumptions similar to those in the previous section, the radial displacement for the $i$th region in the $(n+1)$th loading increment ${}^{n+1}u^i$, which is fully transformed to martensite, can be expressed as:

$${}^{n+1}u^i = {}^{n+1}A_1^i r + \frac{{}^{n+1}A_2^i}{r} - \frac{1}{2}\tilde{g}^i r \ln r + \frac{1}{4}\tilde{g}^i r, \tag{62}$$

where

$$\tilde{g}^i = \frac{\tilde{e}_1^i - \tilde{e}_2^i}{C_{11}^M}. \tag{63}$$

Substitution of (62) into (59) and using the strain-displacement relations gives the stress components in the $i$th fully martensite region as:

$$\begin{aligned} {}^{n+1}\sigma_r = {}& {}^{n+1}A_1^i\left(C_{11}^M + C_{12}^M\right) + \frac{{}^{n+1}A_2^i}{r^2}\left(C_{12}^M - C_{11}^M\right) + C_{11}^M(-\frac{1}{2}\tilde{g}^i \ln r - \frac{1}{4}\tilde{g}^i) \\ & + C_{12}^M(-\frac{1}{2}\tilde{g}^i \ln r + \frac{1}{4}\tilde{g}^i) + \tilde{e}_1^i, \end{aligned} \tag{64}$$

$$\begin{aligned} {}^{n+1}\sigma_\theta = {}& {}^{n+1}A_1^i\left(C_{12}^M + C_{22}^M\right) + \frac{{}^{n+1}A_2^i}{r^2}\left(C_{22}^M - C_{12}^M\right) + C_{12}^M(-\frac{1}{2}\tilde{g}^i \ln r - \frac{1}{4}\tilde{g}^i) \\ & + C_{22}^M(-\frac{1}{2}\tilde{g}^i \ln r + \frac{1}{4}\tilde{g}^i) + \tilde{e}_2^i. \end{aligned} \tag{65}$$

The solution expressed in (64) and (65) is valid from the inner radius up to the annular region in which the martensitic volume fraction is $\xi < 1$. For the other regions, through the outer radius, the solution given in Sect. 5 should be used.

## 7 Solution procedure

Using Eqs. (23) and (24) or Fig. 4, the pressure for initiation of phase transformation in the cylinder is calculated. For any applied pressure below this minimum, the elastic solution is valid and for pressures above this minimum the subsequent procedure should be followed.

The cylinder is divided into $N_1$ narrow annular regions with the $i$th region $r^i < r < r^{i+1}$ (see Fig. 6). The loading is divided into $N_2$ increments. The first increment corresponds to zero internal pressure or any internal pressure for which the whole cylinder is in the austenite phase (see Fig. 4). Assuming that for the $n$th loading increment the solution is known, in the $(n+1)$th increment the following procedure is considered. The radial stress component in the innermost radius is assumed to be ${}^{n+1}\sigma_r^1 = -{}^{n+1}p$ that is the internal pressure corresponding to the $(n+1)$th load increment. As the circumferential stress component is unknown, a typical value ${}^{n+1}\sigma_\theta^1 = \hat{\sigma}$ is assumed for initiating the solution procedure (*e.g.* $\hat{\sigma} = {}^{n}\sigma_\theta^1$). In the plane strain case, the axial stress component $\sigma_z$ in the inner radius is calculated by enforcing the plane strain condition given in (18). Equations (15) and (16) are used for calculating the martensitic fraction $\xi$ at $r = a$. Depending on the calculated martensitic fraction in the inner radius, two cases are possible:

Case I: $0 < \xi^1 < 1$. Equations (48), (49), and (52) are used for calculating the previously introduced constants in the first annular region. By substituting these coefficients into (54) and (55), the unknown constants ${}^{n+1}A_1^1$ and ${}^{n+1}A_2^1$ are calculated. Now, the stress components can be calculated in $r^2$ by means of (54), (55), and by assuming the other parameters to be constants in the first annular region. The calculated stress components for the outer radius of the first region are considered as the stresses in the inner radius of the second region, and the calculations are repeated. In the plane strain case, the axial stress component in the inner radius of each region is calculated by enforcing the condition (18). These calculations are continued up to the last region. Now, the calculated radial stress for the external radius $r = b$ should satisfy the boundary condition $\sigma_r = 0$. If this condition is not satisfied, the assumed circumferential stress in the innermost region ($\hat{\sigma}$) is corrected (e.g. by a fraction of residual radial stress at the external boundary[4]) and the procedure is repeated until satisfaction of the stress boundary condition at $r = b$. As it will be shown in the numerical results, the number of iterations for achieving the consistent stress distribution is small. Note that if in any region in $a < r < b$ the martensitic fraction becomes zero, the solution procedure should be switched to an elastic solution by eliminating the last term in (53) and the last two terms in (54) and (55).

Case II: $\xi^1 = 1$. As was explained in Sect. 6, to obtain the solution in this case, for each annular region, the special step in which that region is fully converted to martensite should be obtained (using (15) and (16)). In this special load increment the method explained in Sect. 6 and Fig. 7 is used for calculating the parameters $(\tilde{\epsilon}_r^t)^i$ and $(\tilde{\epsilon}_\theta^t)^i$. For any annular region in which the material is fully transformed to martensite, the previous procedure of Case I should be used by replacing (48), (49), (52), (54), and (55) by (60), (61), (63), (64), and (65), respectively. Note that, at the inner radius of each narrow annular region, the martensitic volume fraction is calculated, and when it becomes less than 1, the solution is switched to that of Case I.

## 8 Numerical results

In this section, the SMA thick-walled cylinder shown in Fig. 1 is considered with $a$=0.1m, $b$=0.3m and $T$=315K. The outer radius is chosen three times the inner radius for satisfying the thick-walled condition for the cylinder. The cylinder is subjected to different internal pressures, and the stress distribution is calculated using the proposed semi-analytic method in both plane stress and plane strain conditions.

First, a sensitivity analysis is performed for calculating the appropriate number of annular regions $N_1$ and load increments $N_2$ (see Appendix A). Based on the sensitivity analysis results, the thickness is divided into $N_1 = 100$ annular regions (see Fig. 6) and the load is applied in $N_2 = 20$ increments. All the material properties used in the following numerical examples are presented in Table 1, which are taken from [32].

For validation purposes, three dimensional constitutive relations of Sect. 2 are used, and an appropriate user subroutine (UMAT) has been written by FORTRAN in the commercially available finite element program ABAQUS that enables this code to model SMA structures using solid elements. For modeling SMA

[4] For the numerical results presented in this paper, in the $k$th iteration ${}_k\hat{\sigma} = {}_{k-1}\hat{\sigma} - 0.1({}_{k-1}\sigma_r)_{r=b}$, where the left subscripts are used for indicating the iteration number. Using this method and by considering a tolerance of $0.1MPa$ for the residual radial stress at the outer radius, the boundary condition in the outer radius is satisfied for all the case studies in less than 10 iterations.

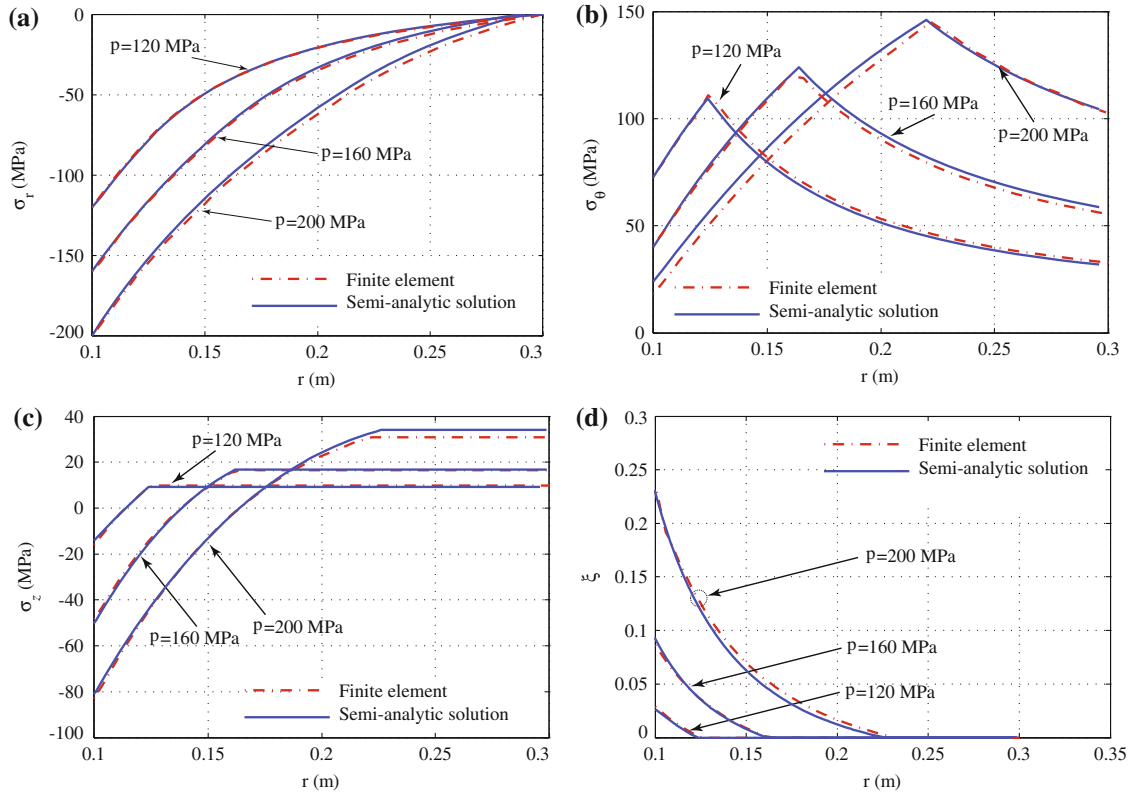


**Fig. 8** Distribution of **a** radial stress, **b** circumferential stress, **c** axial stress, and **d** martensitic volume fraction for an SMA thick-walled cylinder under internal pressure in plane strain with $0 < \xi < 1$ at the inner radius

thick-walled cylinders by 3D solid elements, a 15° sector of a short thick-walled cylinder is considered. The axisymmetric boundary conditions are imposed by constraining the boundary nodes from moving along the circumferential direction. For modeling the plane stress condition, both ends of the cylinder are free in moving along the axial direction and the plane strain condition is imposed by constraining both ends in the axial direction. The developed finite element code is validated by comparing with the previously reported works for SMA structures, e.g. uniaxial tension, bending of beams, and deflection analysis of cylindrical panels [22]. Quadratic (20 node cubic) elements are used. One element is considered along the circumferential and axial directions and the thickness is divided into 30 elements. The pressure loading is divided into 100 steps and the tolerance of $1 \times 10^{-6}$ is considered for the convergence of transformation function (see [22]). A sensitivity analysis is presented in Appendix A for studying the effect of changing the number of elements and load increments on the finite element simulation results.

Three different values of internal pressure are considered for the first case in Sect. 7. Figure 8a shows the radial stress distribution for the internal pressures $p = 120$, 160, and 200 MPa in plane strain. In all the cases, the stress boundary condition in the external radius is satisfied with a tolerance of 0.1 MPa in less than ten iterations (see Sect. 7 for the solution procedure). This figure also shows the results obtained by the finite element method for each pressure. The circumferential stress distribution for these values of internal pressure is depicted in Fig. 8b in plane strain. As it is shown in this figure, circumferential stress has an ascending distribution in the region in which material transformation has taken place and consequently follows a descending distribution in the fully austenite region. However, as it will be shown in the following case studies, the circumferential stress distribution does not follow this pattern for all the values of internal pressure. The axial stress component in plane strain condition obtained by the semi-analytic solution is compared with the finite element results in Fig. 8c. Martensitic volume fraction distribution, calculated by the present method, is shown and compared with the finite element results in Fig. 8d. By comparing the results presented in Fig. 8d with the approximate results of Fig. 5, it is seen that the error of Fig. 5 in predicting the boundary of phase transformation for internal pressures $p = 120$, 160, and 200 MPa is 0.8, 11.4, and 27.1 percent, respectively. As expected, the error of calculating the material transformation boundary by considering elastic stress distribution in regions

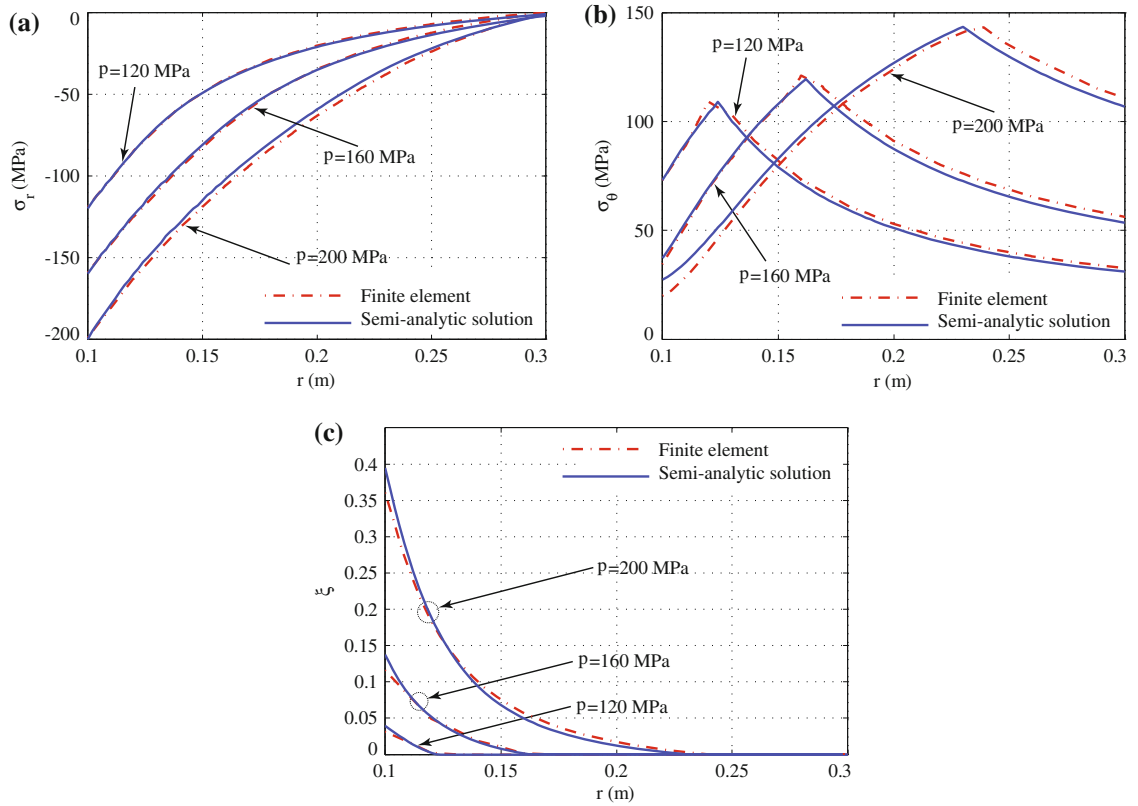


**Fig. 9** Distribution of **a** radial stress, **b** circumferential stress, and **c** martensitic volume fraction for an SMA thick-walled cylinder subjected to internal pressure in plane stress with $0 < \xi < 1$ at the inner radius

with phase transformation (like that presented in Fig. 5) increases by increase in the radius at which material transformation has occurred.

The radial stress distribution, circumferential stress distribution, and martensitic volume fraction in plane stress are shown in Fig. 9. Comparing these distributions in plane stress and plane strain reveals a minor differences in the radial and circumferential stress distributions. It is worth mentioning that for elastic cylinders the radial and circumferential stress distributions are identical in plane stress and plane strain. However, in the present case of an SMA thick-walled cylinder, the phase transformation depends on the three-dimensional state of stress and is affected by the axial stress that exists only in the plane strain case. Therefore, the phase transformation distributions in plane stress and plane strain are not the same. This difference is calculated in (15)–(16) and can clearly be seen by comparing the results in Figs. 8d and 9c. The difference in the phase transformation distribution and the boundary of the region with phase transformation causes a minor difference in the radial and circumferential stress distributions for plane stress and plane strain.

To obtain the internal pressure at which the martensitic volume fraction in the innermost radius reaches $\xi = 1$, a trial and error method is used and the value of this pressure for the present case study is calculated to be $p = 238\,\text{MPa}$ in plane stress and $p = 260\,\text{MPa}$ in plane strain. Distribution of stress components and martensitic volume fraction for these pressures are calculated by the method of Sect. 5 and are depicted in Figs. 10 and 11 for plane strain and plane stress, respectively. For any internal pressure larger than these values, the fully martensite region spreads toward the outer radius and the method of Sect. 6 should be used in any fully transformed annular region. The method of Sect. 6 is used, and distribution of stress components is calculated for $p = 300\,\text{Mpa}$ in both plane stress and plane strain cases (see Sect. 7 for the solution procedure in this case).

For the internal pressure $p = 300$ MPa, a portion of the cylinder is fully transformed to martensite in both plane stress and plane strain conditions. Figure 10 compares the radial, circumferential, and axial stress distributions, and the martensitic volume fraction calculated by the present semi-analytic method and the three-dimensional finite element simulations in the plane strain case. The radial stress, circumferential stress, and martensitic volume fraction distributions for plane stress are shown and compared with the finite element results in Fig. 11.

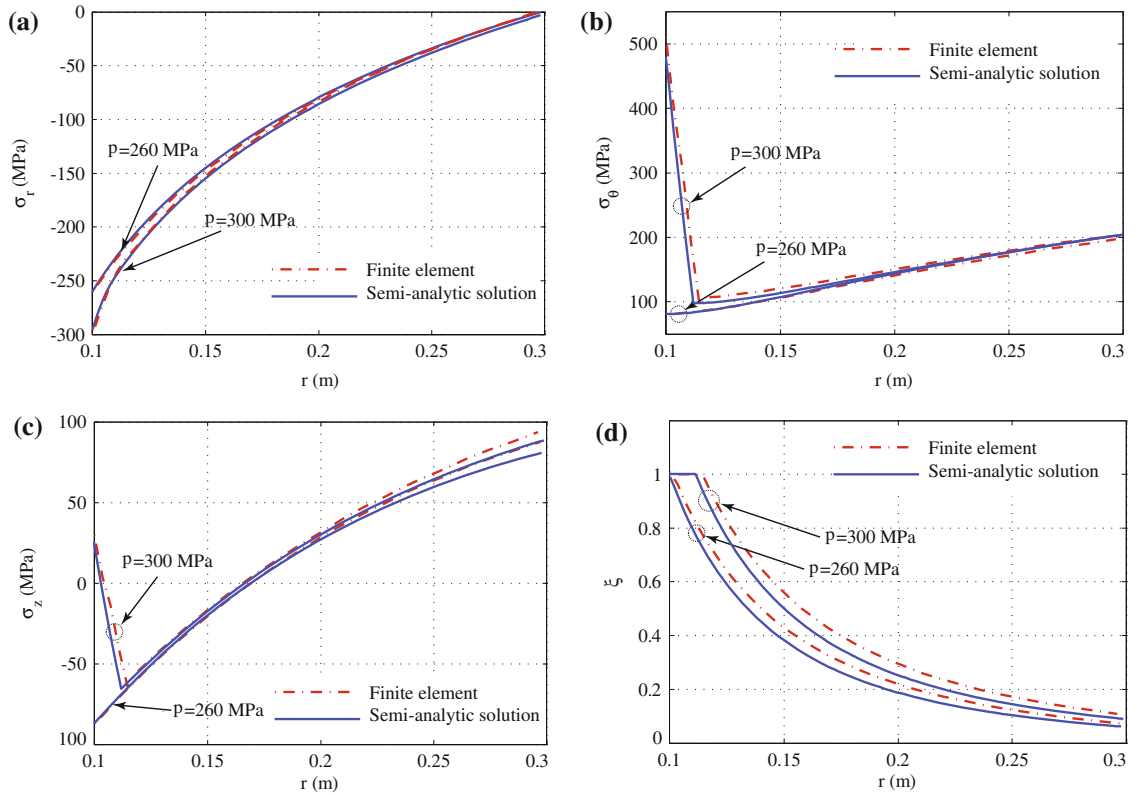


**Fig. 10** Distribution of **a** radial stress, **b** circumferential stress, **c** axial stress, and **d** martensitic volume fraction for an SMA thick-walled cylinder under internal pressure in plane strain with $\xi = 1$ at the inner radius

As it is shown in Figs. 10b and 11b, by spread of the fully martensite region, the circumferential stress distribution in the fully transformed region increases considerably. This phenomenon should be considered in the design of SMA thick-walled pipe joints or pressure vessels. A designer should consider that any internal pressure that causes a portion of the cylinder to be fully transformed to martensite will produce an extremely large circumferential stress in the inner radius that should preferably be avoided. Figure 10c shows the axial stress distribution in the plane strain case. As it is shown, the present method of enforcing the plane strain condition for calculating the axial stress component leads to a good agreement between the semi-analytic and numerical simulation results. Distribution of martensitic volume fraction is shown in Figs. 10d and 11c for plane strain and plane stress, respectively. As it is shown in these figures, for $p = 300\,\text{MPa}$ an annular region attached to the inner radius is completely converted to martensite ($\xi = 1$). As explained in Sect. 6 and depicted in Fig. 7, in the present semi-analytic solution, an approximation is used for finding the values of transformation strains in the region that is completely converted to martensite. In order to study the accuracy of this approximation, the values of transformation strain components in plane stress are calculated for internal pressure $p = 300\,\text{MPa}$. These values are compared with the results of finite element simulations in Fig. 11d. As it is seen, the present method predicts the transformation strains in good agreement with the finite element results. So it can be concluded that choosing an appropriate number of load steps in the semi-analytic solution, the proposed approximation will not affect the results. Looking at Figs. 8–11 reveals the acceptable agreement between the numerical simulation results and the present semi-analytic solution. It is worth mentioning that the results of the present method are obtained without a massive computation in contrast to the finite element (or other numerical simulations) that require a massive iterative computational process. Since the semi-analytic solution is not affected by those parameters that may make a numerical simulation ill-conditioned (e.g. the number of loading steps and the number of convergence iterations in satisfying the constitutive equation (see [32]) or the number of equilibrium iterations in the non-linear finite element simulation[5]), we believe that our

[5] In the present case studies, the finite element simulation in each load increment (loading was divided into 100 increments) needs up to 20 iterations for satisfying the constitutive equations convergence criteria with a tolerance of $1 \times 10^{-6}$ for the convergence of transformation function (see [32] and [22]). Since the geometry and loading are axisymmetric, the elements in the

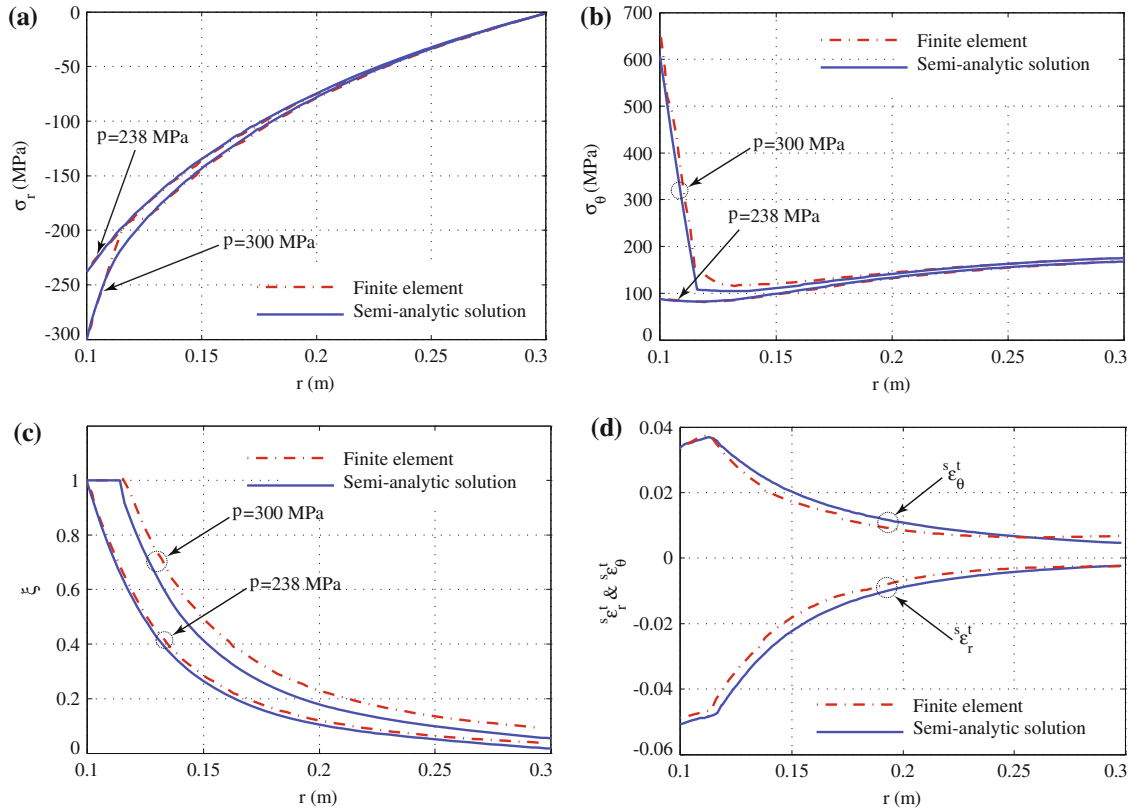


**Fig. 11** Distribution of **a** radial stress, **b** circumferential stress, **c** martensitic volume fraction, and **d** transformation strain components for an SMA thick-walled cylinder under internal pressure in plane stress with $\xi = 1$ at the inner radius

method can be used for validating the accuracy of numerical methods like finite element method in modeling shape memory alloy structures.

## 9 Conclusions

A semi-analytic solution is presented for the analysis of shape memory alloy thick-walled cylinders subjected to internal pressure in both plane stress and plane strain conditions. First, a two-dimensional reduction of Boyd–Lagoudas's polynomial SMA constitutive model is obtained for both plane stress and plane strain. Then, the thick-walled cylinder is divided into a finite number of narrow annular regions, and the loading is partitioned into a finite number of increments. Appropriate assumptions are made in each region in order to find a closed-form solution for the equilibrium equations in terms of radial displacements within the regions in which the phase transformation has started but has not completed. Considering the history of loading and the final values of transformation strain components, another solution is given for those regions and load increments for which the material is completely transformed to martensite. By satisfying the continuity condition at the interfaces between the annular regions and the boundary conditions at the inner and outer radii, a semi-analytic solution is obtained for any value of internal pressure. Several numerical examples are presented for different loading phases, and the results of the proposed solution are compared with those of three-dimensional finite element simulations in both plane stress and plane strain cases. In contrast with finite element simulations, the results of the present semi-analytic solution are not severely affected by the number of load steps, and they are independent of the criteria for satisfaction of the constitutive relation convergence, and the number of iterations for convergence in considering geometric non-linearities. Considering the numerical stability of the present semi-analytic method, we believe that it can be used in validating the results of common numerical methods in analyzing shape memory alloy structures.

Footnote 5 continued
finite element model are not distorted significantly and less than five iterations were performed for the equilibrium satisfaction due to the non-linear geometry in the finite element model.

## Appendix 1: Sensitivity of numerical results to the number of annular regions and load increments in the semi-analytic solution and the number of elements and load increments in the finite element simulations

A sensitivity analysis is performed for choosing the appropriate number of annular regions $N_1$ and load increments $N_2$ in the semi-analytic solution and the number of elements and load increments in the finite element simulations. The stress components are considered to be converged when the maximum difference is smaller than 0.1 MPa, and the martensitic volume fraction convergence is achieved when the maximum difference is smaller than 0.001. Figure 12a shows the effect of increasing the number of annular regions on the martensitic volume fraction distribution in the plane strain case for $p = 200$ MPa and with considering 20 load increments. The convergence is achieved with 100 annular regions for the martensitic volume fraction. The convergence of the circumferential stress in this case for 100 annular regions is shown in Fig. 12b. The convergence for radial stress distribution is achieved with 50 annular regions. Our numerical tests show that $N_1 = 100$ is the optimum value.

Figure 13a shows the effect of increasing the number of loading increments on the martensitic volume fraction distribution in the plane strain case for $p = 200$MPa when the number of annular regions is $N_1 = 100$. Convergence is achieved with 10 load increments for the martensitic volume fraction. Convergence of the circumferential stress in this case is achieved with 20 load increments as shown in Fig. 13b. Convergence for radial stress distribution is achieved with 10 annular regions. It is seen that $N_2 = 20$ is the optimum value. The convergence study for the plane stress case leads to the same optimum number of annular regions and load increments.

Figure 14 shows the effect of the number of finite elements on the finite element simulation results for the martensitic volume fraction and circumferential stress component in the plane stress case. As it is shown, results are not sensitive to the number of elements. The same analysis is performed for all the parameters, and

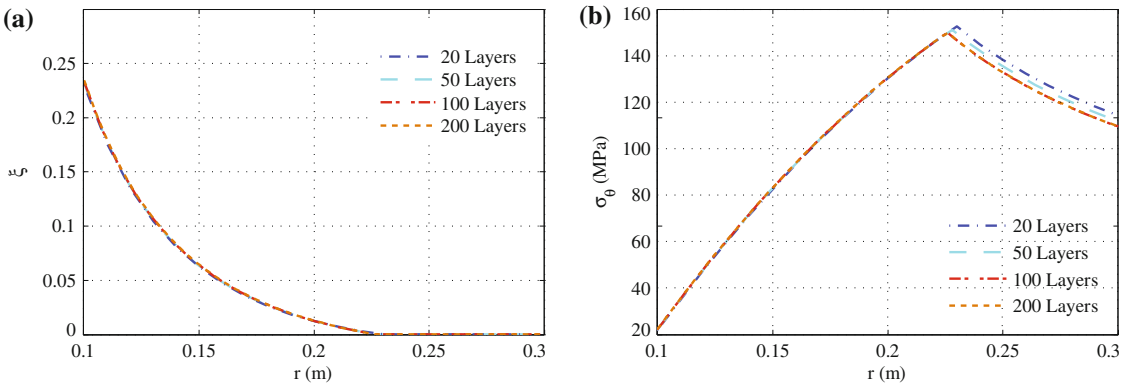


**Fig. 12** The effect of the number of annular regions in the semi-analytic solution on **a** martensitic volume fraction, and **b** circumferential stress in the plane strain case ($p = 200$ MPa and 20 load increments)

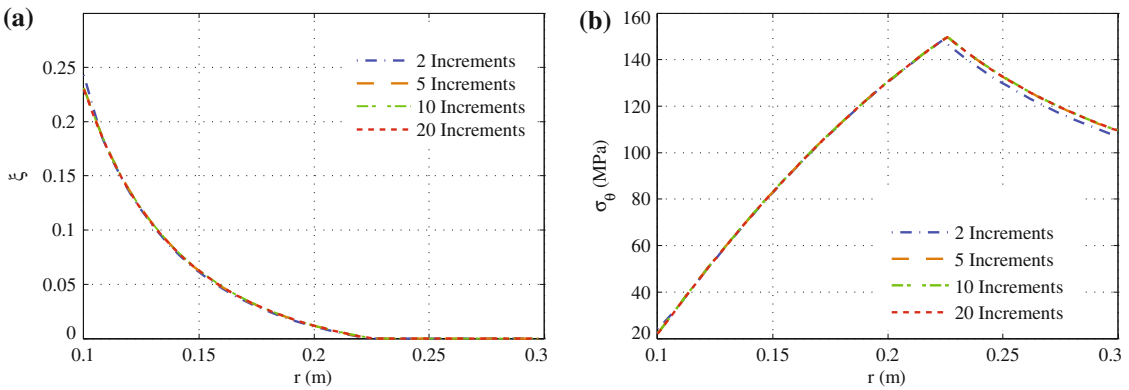


**Fig. 13** The effect of the number of load increments in the semi-analytic solution on **a** martensitic volume fraction, and **b** circumferential stress in the plane strain case ($p = 200$ MPa and 100 annular regions)

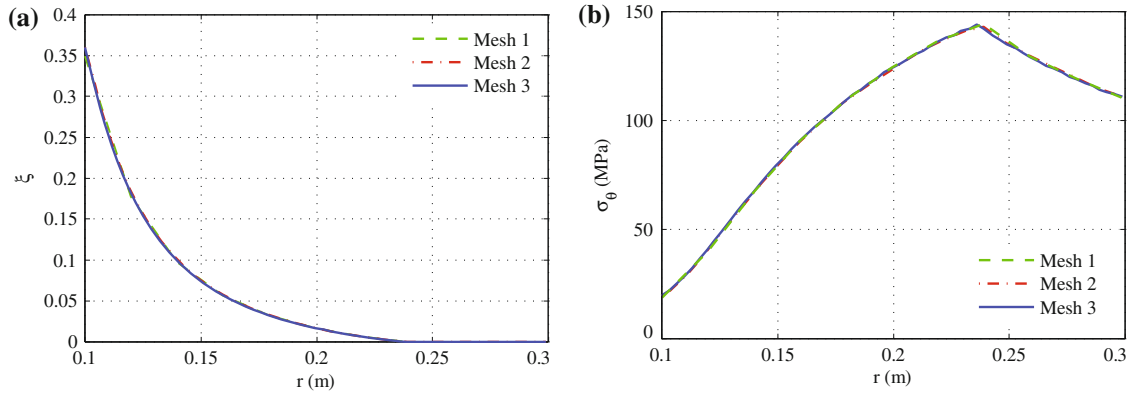


**Fig. 14** The effect of the number of elements in the finite element simulation on **a** martensitic volume fraction, and **b** circumferential stress in the plane stress case for Mesh 1: $10 \times 1 \times 1$ elements (in $r$, $\theta$ and $z$ directions), Mesh 2: $30 \times 1 \times 1$ elements, and Mesh 3: $60 \times 2 \times 1$ elements ($p = 200$ MPa and 100 load increments)

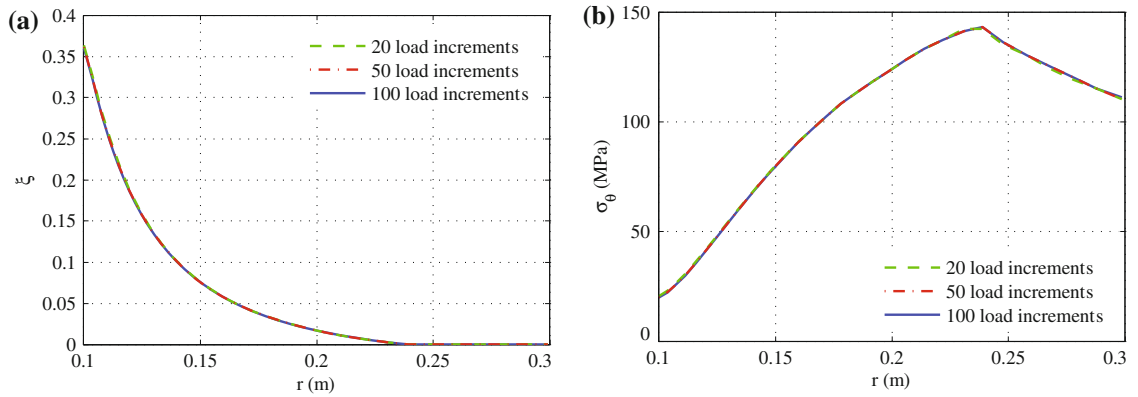


**Fig. 15** The effect of the number of the load increments in the finite element simulations on **a** martensitic volume fraction, and **b** circumferential stress in plane stress ($p = 200$ MPa and $30 \times 1 \times 1$ elements in $r$, $\theta$ and $z$ directions)

Mesh 2 (see the caption of Fig. 14 for mesh definitions) with $30 \times 1 \times 1$ elements in $r$, $\theta$, and $z$ directions is considered for all the studies presented in this paper (20 node cubic elements are used in all cases).

In order to find the appropriate number of load increments in the finite element simulations, a sensitivity analysis for the number of load increments is performed for all the parameters. Figure 15 shows the effect of load increment numbers on the volume fraction and circumferential stress component in the plane stress case. As it is seen, the finite element simulation results are not sensitive to the number of load increments as well. It is worth mentioning that the history of these parameters as a function of internal pressure is highly affected by the load increment numbers. For all the case studies presented in this paper, 100 load increments are considered. The same sensitivity analysis for the plane strain case and for the other parameters is performed, and the results are very similar to those of plane stress.

## References

1. Birman, V.: Analysis of an infinite shape memory alloy plate with a circular hole subjected to biaxial tension. Int. J. Solids Struct. **36**, 167–178 (1999)
2. Bo, Z., Lagoudas, D.C.: Thermomechanical modeling of polycrystalline SMAs under cyclic loading, Part I: theoretical derivations. Int. J. Eng. Sci. **37**, 1089–1140 (1999)
3. Boresi, A.P., Schmidt, R.J.: Advanced Mechanics of Materials, 6th ed. Wiley, Hoboken (2003)
4. Boyd, J.G., Lagoudas, D.C.: A thermodynamic constitutive model for the shape memory alloy materials. Part I. the monolithic shape memory alloy. Int. J. Plast. **12**, 805–842 (1996)
5. Brook, G.B.: Applications of titanium–nickel shape memory alloys. Mater. Des. **4**(4), 835–840 (1983)
6. DesRoches, R., Smith, B.: Shape memory alloys in seismic resistant design and retrofit: a critical review of their potential and limitations. J. Earthquake Eng. **8**, 415–429 (2004)
7. Feng, X.Q., Sun, Q.P.: Shakedown analysis of shape memory alloy structures. Int. J. Plast. **23**(2), 183–206 (2004)

8. Feng, X.Q., Sun, Q.P.: In situ profilometry for non-uniform strain field measurement of NiTi shape memory alloy microtubing under complex stress states. Smart Mater. Struct. **16**(1), S179–S186 (2007)
9. Forsythe, G.E., Malcolm, M.A., Moler, C.B.: Computer Methods for Mathematical Computations. Prentice-Hall, Englewood Cliffs (1976)
10. Hartl, D.J., Lagoudas, D.C.: Aerospace applications of shape memory alloys. Proc. Inst. Mech. Eng. G J. Aerosp. Eng. **221**, 535–552 (2007)
11. He, Y.J., Sun, Q.P.: Scaling relationship on macroscopic helical domains in NiTi tubes. Int. J. Solids Struct. **46**, 4242–4251 (2009)
12. Jee, K.K., Hana, J.H., Jang, W.Y.: A method of pipe joining using shape memory alloys. Mater. Sci. Eng. A **438**(440), 1110–1112 (2006)
13. Kim, C., Jang, D.H., Choi, H.S.: An externally pressurized elliptic composite cylinder stiffened with activated SMA strips. In: 43rd AIAA/ASME/ASCE/AHS/ASC Structures, Structural Dynamics, and Materials Conference, pp. 22–25. Denver, Colorado (2002)
14. Kuribayashi, K., Tsuchiya, K., You, Z., Tomusb, D., Umemotob, M., Ito, T., Sasaki, M.: Self-deployable origami stent grafts as a biomedical application of Ni-rich TiNi shape memory alloy foil. Mater. Sci. Eng. A **419**, 131–137 (2006)
15. Lagoudas, D.C., Bo, Z., Qidwai, M.A.: A unifed thermodynamic constitutive model for SMA and finite element analysis of active metal matrix composite. Mech. Compos. Mater. Struct. **3**, 153–179 (1996)
16. Lagoudas, D.C., Ravi-Chandar, K., Sarh, K., Popov, P.: Dynamic loading of polycrystalline shape memory alloy rods. Mech. Mater. **35**, 689–716 (2003)
17. Lagoudas, D.C. (ed.): Shape memory alloys: modeling and engineering applications. Springer, New York (2008)
18. Langelaar, M., Keulen, F.V.: Modeling of a shape memory alloy active catheter. In: 45th AIAA Structures, Structural Dynamics and Materials Conference, pp. 19–22. Palm Springs, Calofornia (2004)
19. Li, Z.Q., Sun, Q.P.: The initiation and growth of macroscopic martensite band in nano-grained NiTi microtube under tension. Int. J. Plast. **18**, 1481–1498 (2002)
20. Liang, C., Rogers, C.A.: The multi-dimensional constitutive relations of shape memory alloys. J. Eng. Math. **26**, 429–443 (1992)
21. Machado, L.G., Savi, M.A.: Medical applications of shape memory alloys. Braz. J. Med. Biol. Res. **36**, 683–691 (2003)
22. Mirzaeifar, R., Shakeri, M., Sadighi, M.: Nonlinear finite element formulation for analyzing shape memory alloy cylindrical panels. Smart Mater. Struct. **18**(3), 035002 (2009)
23. Mirzaeifar, R., DesRoches, R., Yavari, A.: Exact solutions for pure torsion of shape memory alloy circular bars. Mech. Mater. 42(8), 797–806 (2010)
24. Müller, I., Xu, H.: On the pseudo-elastic hysteresis. Acta Metal. Mater. **39**(3), 263–271 (1991)
25. Müller, I., Seelecke, S.: Thermodynamic aspects of shape memory alloys. Math. Comput. Model. **34**(12-13), 1307–1355 (2001)
26. Paine, J.S.N., Rogers, C.A., Smith, R.A.: Adaptive composite-materials with shape-memory alloy actuators for cylinders and pressure-vessels. J. Intell. Mater. Syst. Struct. **6**(2), 210–219 (1995)
27. Paine, J.S.N., Rogers, C.A.: Using the adaptive SMA composite cylinder concept to reduce radial dilation in composite pressure vessels. In: Chopra, I. (ed.) Smart Structures and Materials 1995: Smart Structures and Integrated Systems, Proc. SPIE, vol. 2443, pp. 195–205
28. Patoor, E., Barbe, P., Eberhardt, A., Berveiller, M.: Thermomechanical behavior of shape memory alloys. Arch. Mech. **40**, 775–794 (1988)
29. Patoor, E., Lagoudas, D.C., Entchev, P.B., Brinson, L.C., Gao, X.: Shape memory alloys, part I: general properties and modeling of single crystals. Mech. Mater. **38**, 391–429 (2006)
30. Petrini, L., Migliavacca, F., Massarotti, P., Schievano, S., Dubini, G., Auricchio, F.: Computational studies of shape memory alloy behavior in biomedical applications. J. Biomech. Eng. **127**, 716–725 (2005)
31. Qidwai, M.A., Lagoudas, D.C.: On thermomechanics and transformation surfaces of polycrystalline NiTi shape memory alloy material. Int. J. Plast. **16**, 1309–1343 (2000)
32. Qidwai, M.A., Lagoudas, D.C.: Numerical implementation of a shape memory alloy thermomechanical constitutive model using return mapping algorithms. Int. J. Numer. Methods Eng. **47**, 1123–1168 (2000)
33. Tanaka, K.: A phenomenological description on thermomechanical behavior of shape memory alloys. ASME J. Pressure Vessel Technol. **112**, 158–163 (1990)
34. Tanaka, K., Nishimura, F., Hayashi, T., Tobushi, H., Lexcellent, C.: Phenomenological analysis on subloops and cyclic behavior in shape memory alloys under mechanical and/or thermal loads. Mech. Mater. **19**, 281–292 (1995)
35. Xua, M.B., Song, G.: Adaptive control of vibration wave propagation in cylindrical shells using SMA wall joint. J. Sound Vib. **278**, 307326 (2004)